applied optics

Advanced laser development and plasma-physics studies on the multiterawatt laser

I. A. Begishev,[1,*] V. Bagnoud,[2] S.-W. Bahk,[1] W. A. Bittle,[1] G. Brent,[1] R. Cuffney,[1]
C. Dorrer,[1] D. H. Froula,[1] D. Haberberger,[1] C. Mileham,[1] P. M. Nilson,[1]
A. V. Okishev,[1,†] J. L. Shaw,[1] M. J. Shoup III,[1] C. R. Stillman,[1,3] C. Stoeckl,[1]
D. Turnbull,[1] B. Wager,[1] J. D. Zuegel,[1] and J. Bromage[1]

[1]Laboratory for Laser Energetics, University of Rochester, 250 East River Road, Rochester, New York 14623-1299, USA
[2]GSI-Helmholtzzentrum für Schwerionenforschung GmbH, Planckstraße 1, 64291 Darmstadt, Germany
[3]Image Science, Space and Airborne System, L3Harris Technologies, Inc., 332 Initiative Drive, Rochester, New York 14624, USA
*Corresponding author: ibeg@lle.rochester.edu

The multiterawatt (MTW) laser, built initially as the prototype front end for a petawatt laser system, is a 1053 nm hybrid system with gain from optical parametric chirped-pulse amplification (OPCPA) and Nd:glass. Compressors and target chambers were added, making MTW a complete laser facility (output energy up to 120 J, pulse duration from 20 fs to 2.8 ns) for studying high-energy-density physics and developing short-pulse laser technologies and target diagnostics. Further extensions of the laser support ultrahigh-intensity laser development of an all-OPCPA system and a Raman plasma amplifier. A short summary of the variety of scientific experiments conducted on MTW is also presented. © 2021 Optica Publishing Group

1. INTRODUCTION

Fundamental research in high-energy-density physics [1] and materials science [2] has accelerated the development of kilojoule and megajoule lasers [3–9]; however, the deployment of these lasers is limited because of the cost and complexity of construction and operation. Low repetition rates (typically a few shots per day) hinder the mapping of large parameter spaces and statistical averaging. Midscale lasers producing hundreds of joules with subpetawatt peak power at higher repetition rates provide more flexibility and enhanced user access. Lasers at this scale enable technologies to be developed and tested before they are implemented on large-scale facilities. They also serve as experimental platforms for scientific research in their own right.

This paper describes the multiterawatt (MTW) laser at the Laboratory for Laser Energetics (LLE), a midscale laser system built initially as the prototype front end for OMEGA EP [4]. Currently, the MTW operates at 1053 nm, where gain is provided by a combination of optical parametric amplification in nonlinear crystals and laser amplification in neodymium-doped glass. A pulse compressor and three target chambers were added, enabling MTW to serve as a complete user facility for plasma physics research, a platform for the development of laser technologies and target diagnostics as well as a system for large-area damage testing. MTW can be configured to pump the high-energy stage of an all-OPCPA laser system, a promising

approach to produce ultra-intense pulses ($>10^{23}$ W/cm^2). The MTW is also available to external users for experimental campaigns.

A block diagram of the MTW laser is shown in Fig. 1. The MTW laser is a complex system with narrowband and broadband arms, which can be combined or work separately for different applications.

For broadband operation, separate broadband and narrowband front ends produce synchronized, nanosecond pulses for the optical parametric chirped-pulse-amplified (OPCPA) seed and pump, respectively. The narrowband pulse is amplified in three Nd:YLF amplifiers and frequency doubled before it pumps the OPCPA crystals. The resulting broadband signal pulse is further amplified in two Nd:glass amplifiers. After the picosecond compressor, pulses can be directed to the spherical target chamber (STC), the cylindrical target chamber (CTC), or the underdense plasma (UDP) chamber. As an option, the picosecond compressor can be bypassed to allow nanosecond pulses to propagate directly to each target chamber.

For narrowband operation, the output of the Nd:YLF amplifiers goes directly to the Nd:glass amplifiers. This mode is mainly used to pump the final stage of an ultrabroadband optical parametric amplifier line (OPAL) after second-harmonic generation. This supports the generation of >10 J, >140 nm pulses [10], which are compressed in the femtosecond compressor and delivered to the UDP chamber. Table 1 summarizes the
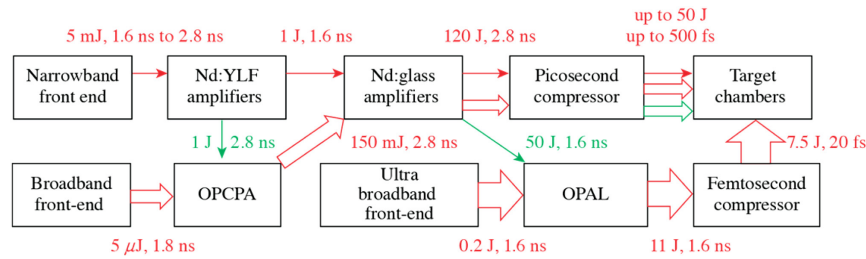
Fig. 1. Multiterawatt (MTW) laser block diagram. OPCPA, optical parametric chirped-pulse amplifier; OPAL, optical parametric amplifier line.

Table 1. Parameters and Main Applications of the MTW Laser

| Mode	Application	λ (nm)	E (J)	τ (ps)
Broadband	Large-area damage tests	1053	120	2400
	High-energy-density physics, x-ray, and neutron diagnostics	1053, 527	35–50	0.5–100
	Raman plasma amplification	1053, 527	35–40	0.5–100
	Ultrafast streak-camera development	1053, 264	0.1 (5 Hz)	0.5–100
Narrowband	Pump for all OPCPA laser	527	50	1600
	5ω generation development	527, 263, 211	1.2 (5 Hz)	1000–2800
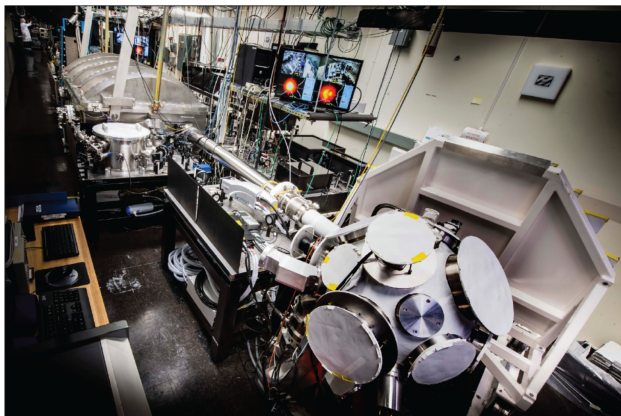
Fig. 2. General view of the MTW laser system from the spherical target chamber side.

range of parameters (central wavelength λ, energy E, and pulse duration τ) and applications of the broadband and narrowband modes of operation for the MTW laser system. A general view of the MTW laser from the end of the system shows the picosecond grating compressor chamber (ps-GCC), the STC, and the CTC (Fig. 2).

This paper details the MTW laser and describes technologies used in its creation (Section 2), demonstrates major diagnostics to characterize MTW system's parameters (Section 3), and provides a short overview of its main scientific applications (Section 4).

2. LASER DESCRIPTION

The detailed layout of the MTW laser is shown in Fig. 3. Depending on the desired operation mode, switchyards 1 to 5 (indicated as blue spots) using mirrors on kinematic or translation stages send beams along different paths. The broadband

front end consists of a commercial femtosecond master oscillator, an ultrafast optical parametric amplifier (UOPA) for better temporal contrast, and a pulse stretcher. The narrowband front end includes a pulse-shaping system, a diode-pumped regenerative amplifier (regen), and a crystal large-aperture ring amplifier (CLARA), all operating at 1053 nm. The amplified narrowband beam is frequency-converted to the second harmonic to pump the OPCPA stages, which are seeded by the broadband front end. The OPCPA output signal beam is shaped using a programmable spatial light modulator (PSLIM) and amplified in a Nd:glass rod amplifier (RA) and disk amplifier (DA). The pulse is compressed in the ps-GCC and can be delivered to one of three target chambers. For solid-target experiments, the STC or CTC are typically used. Gas-jet and gas-cell experiments are conducted in the UDP chamber.

In the narrowband operation mode, the switchyard mirrors directly send the CLARA output beam to the RA and DA for amplification. To pump the final noncollinear optical parametric amplifier (NOPA5) for the OPAL system, Switchyard 3 is used to send the pulse to the second-harmonic-generation table (SHG) before propagating to the NOPA5 area. Here, it is overlapped in time and space at the OPCPA crystal with the ultrabroadband seed pulse from the OPAL front end [10]. The amplified signal pulse is compressed in the femtosecond grating compressor chamber (fs-GCC) and sent to the UDP chamber.

The narrowband mode has also been used to develop technologies for the fifth-harmonic generation of joule-class, near-infrared pulses. For this, the CLARA output can be sent with or without amplification in the RA to the 5ω table, where several studies using cascades of nonlinear crystals have been performed [11,12].
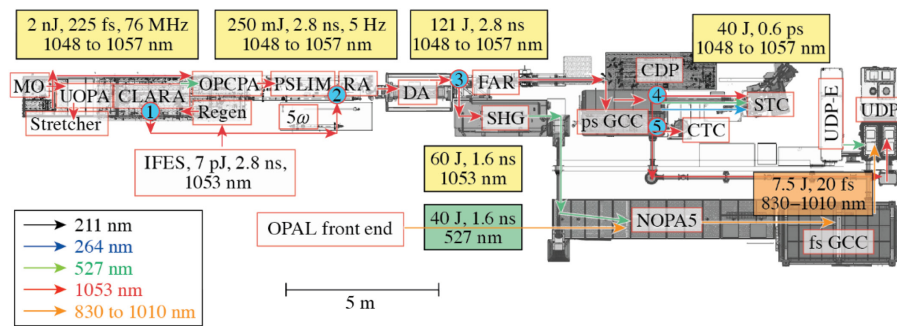
Fig. 3. MTW laser layout. MO, master oscillator; UOPA, ultrafast optical parametric amplifier; CLARA, crystal large-aperture ring amplifier; IFES, integrated frond-end system; PSLIM, programmable spatial light modulator; RA, rod amplifier; 5ω, fifth-harmonic-generation table; DA, disk amplifier; FAR, Faraday isolator; SHG, second-harmonic-generation table; GCC, grating compressor chamber; CDP, compressor diagnostics package; STC, spherical target chamber; CTC, cylindrical target chamber; NOPA5, the fifth nonlinear optical parametric amplifier stage; UDP, underdense plasma chamber; UDP-E, UDP laser; 1–5, switchyards.

A. Hardware Timing System

The hardware timing system enables end-to-end synchronization of all laser components and experimental diagnostics. A high-precision analog sinusoidal reference frequency generator at 38 MHz ($37, 998, 935 \pm 15$ Hz) serves as the clock for a master timing generator and several timing crates. Each crate contains a number of multichannel delay modules that provide transistor-transistor logic (TTL) pulses for triggering the laser and experimental systems.

The master timing generator provides derived rates for video synchronization as well as the 0.1 Hz timing pulse and trigger pulses that occur 10 s before a laser shot (T-10) and synchronously with the shot (T-0). The delay modules in the timing crates provide synchronized channels at 5 and 300 Hz with precise delays: for example, a 300 Hz rate is used for the narrowband fiber front end and a 5 Hz trigger is used for the Nd:YLF regenerative amplifier and the ring amplifier. A web-based control interface permits operators to select the trigger rate and the delay for each channel independently. The reference frequency generator also generates the frequency-doubled analog sinusoidal signals at 76 MHz to synchronize the mode-locked master oscillator of the broadband front end. The timing jitter of optical pulses is ~5 ps rms relative to the reference clock.

B. Integrated Front-End System

The integrated front-end system generates shaped pulses for each mode of the MTW operation with high stability, turn-key operation, and low maintenance [13]. It starts from a compact, stable, single-frequency distributed feedback commercial fiber laser (Adjustic/Koheras). This 10 mW continuous-wave (cw) laser is wavelength-stabilized to the gain peak of the main Nd:YLF amplifiers (~1053 nm) via temperature control of an intracavity fiber Bragg grating. The exact wavelength is tuned to match the unseeded emission from the Nd:YLF regen, which depends slightly (~0.2 nm) on humidity-sensitive optics and the temperature of the gain crystal.

An integrated unit composed of two lithium-niobate ($LiNbO_3$) Mach–Zehnder modulators is used for pulse-shaping. The first Mach–Zehnder modulator is driven by a Kentech arbitrary waveform generator that carves a shaped
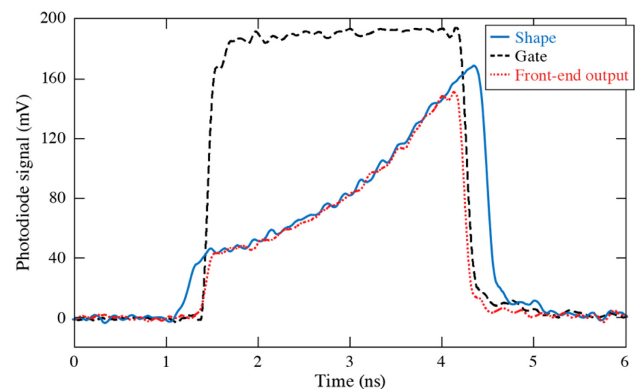

Fig. 4. Front-end pulse shapes, corresponding to operation of the first modulator only ("shape"), the second modulator only ("gate"), and both modulators ("front-end output").

optical pulse out of the cw output from the fiber laser. The second Mach–Zehnder modulator is driven by a square pulse generator to increase the temporal contrast of the optical pulse by temporal gating. The arbitrary waveform generator has a 100 ps sample separation for creating pulse shapes that are precompensated for the transmission nonlinearity of the $LiNbO_3$ modulator and the square-pulse distortion of the regen and CLARA. This programmable control is critical for setting the temporal profile of the OPCPA pump pulse and, therefore, the bandwidth of the OPCPA amplifiers for MTW and OPAL. A library of tens of pulse shapes allows easy modification of the output pulse shape for different applications. A picojoule pulse from the $LiNbO_3$ modulator is amplified in a high-gain (23 dB) polarization-maintaining, double-pass, ytterbium-doped fiber amplifier for seeding the regen. Figure 4 shows examples of output pulses for the standard OPCPA configuration, for which pulse shaping allows for the generation of an amplified 2.8 ns flat-in-time super-Gaussian pump pulse by precompensation of square-pulse distortion in the laser amplifiers.

C. Regenerative Amplifier

The regenerative Nd:YLF amplifier (regen) is a key subsystem for providing high gain at 1053 nm with a TEM_{00} Gaussian output spatial beam profile. A fiber-coupled cw diode array is

operated in the pulsed regime for end pumping the Nd:YLF crystal. Two 25 W or one 50 W fiber-coupled diode arrays are used with a center wavelength of 805 nm, and the pump is delivered to the regen module via a 3 m long, 800 μm core step-index multimode fiber. The radial symmetry of the fiber output after collimation enables the pumped region to be matched to the resonator's fundamental mode in the crystal.

The regen has a linear, semiconfocal, 2 m long folded resonator with the switching time of the Pockels cell <9 ns. The roundtrip number is set to 64 as a compromise between higher output energy and lower pulse distortion. The maximum output energy at 2.8 ns pulse is 6 mJ. Excellent long-term (24 h) output-pulse-energy stability of better than 1% rms fluctuations has been achieved with excellent beam quality (<1% ellipticity) [14].

D. Crystal Large-Aperture Ring Amplifier

The CLARA is used to amplify the regen output to an energy level suitable either for pumping a pair of OPCPA stages in the broadband mode or for injection into the Nd:glass amplifiers in the narrowband mode. A limited number of gain media are suitable for this. Because MTW was built as a prototype front end for the kilojoule OMEGA EP laser system [4], a 5 Hz repetition rate was required to align its main amplifiers and numerous diagnostics. This repetition rate poses challenges for joule-scale, flash-lamp-pumped Nd:glass amplifiers because of the thermal load and degradation of the amplified beam. Instead, Nd:YLF was selected because it matches the gain peak of Nd-doped phosphate laser glasses and has relatively high thermal conductivity with low thermal astigmatism. Water cooling of the 25.4 mm diameter, 110 mm long rods is sufficient to support joule-scale pulses at 5 Hz.

The transmitted wavefront quality of commercially available, large-aperture Nd:YLF laser rods was dramatically improved by magnetorheological finishing (MRF) [15]. Two Nd:YLF rods were polished on one face using MRF to compensate for bulk inhomogeneities that cause the transmitted wavefront errors, while the other surface was polished flat. Typical values of wavefront errors for uncorrected rods exceed 0.5λ. The

MRF-corrected rods have transmitted wavefront errors <0.1λ at 1053 nm, which requires about 1 mrad alignment accuracy. Correcting these errors increases the usable aperture of the rods, resulting in a higher energy extraction.

The CLARA architecture is based on a Q-switched, cavity-dumped, self-imaging laser cavity. The Gaussian beam from the regen is expanded to 30 mm (FWHM) and shaped by an apodizer [16], as shown in the insets in Fig. 5. An intracavity four-lens vacuum spatial filter (CLARA VSF) with positive and negative lenses images the apodizer to a plane between the two Nd:YLF rods and reimages this plane onto itself at each round-trip.

A 25.4 mm aperture Pockels cell sets the number of round-trips in the 7 m (21 ns) round-trip cavity. All of the MTW operation modes are met with either three or four round-trips. The output energy for a 14 mm × 14 mm beam is up to 3.2 J. Energy stability of the laser is excellent, achieving better than 0.5% rms and 3.8% peak-to-mean over 10,000 shots at 5 Hz.

E. Second-Harmonic Generator

The CLARA image is relayed to the SHG stage consisting of a lithium triborate crystal (LBO), which was chosen because of its relatively high nonlinearity and angular acceptance. A diagnostics package consisting of beam cameras and energy meters with a Hamamatsu photomultiplier for pulse measurements to characterize and optimize the SHG process. The second-harmonic conversion efficiency typically exceeds 70%. The maximum SHG energy used for pumping the MTW OPCPA stages is kept below 1.1 J. A nominal SHG beam profile is displayed in Fig. 6(a). A typical second-harmonic pulse is shown in Fig. 6(b). The pulse is approximately super-Gaussian with an order $N = 34$ and a duration of 2.8 ns (FWHM). For most MTW applications, the pulse duration is in the 1 to 2.8 ns range. However, the flexibility of the narrowband front end allows the output pulse shape to be optimized, for example, to precompensate pulse distortion in subsequent glass amplifiers or to meet a particular pulse shape requested for experiments.
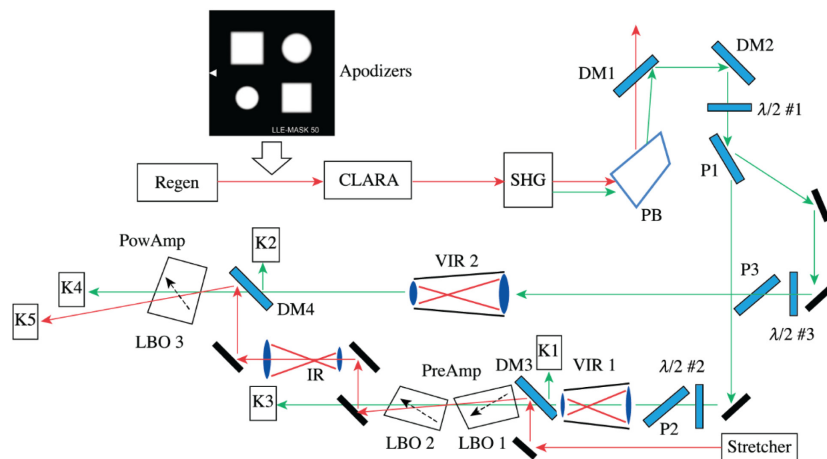

Fig. 5. OPCPA layout. VIR, vacuum image relay; PB, Pellin–Broca prism; DM, dichroic mirror; P, polarizers; λ/2, half-wave plates; LBO, lithium triborate crystals; Preamp, preliminary amplifier; PowAmp, power amplifier; K, calorimeters. Inset: A plate with four apodizers defining a square or round beam of various sizes.
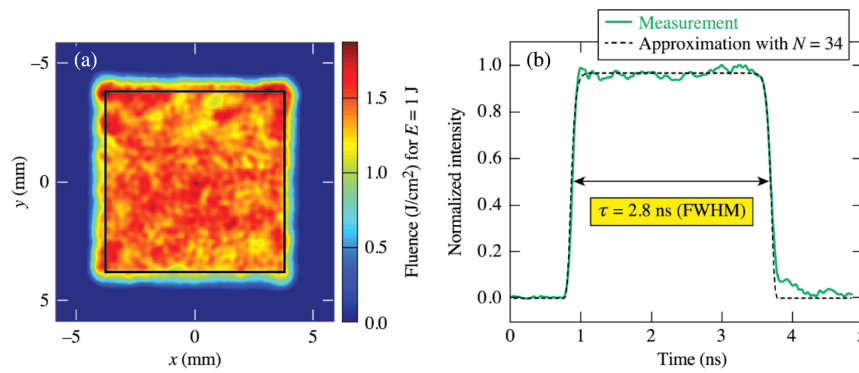
Fig. 6.   Typical second-harmonic (a) beam profile and (b) pulse shape with an approximation by a super-Gaussian shape ($N = 34$).

F. Broadband Front End

The broadband front end is based on a mode-locked laser, providing seed pulses to an optical parametric amplifier pumped by a short optical pulse (Fig. 7). This architecture has been demonstrated as a means to significantly improve the temporal contrast of optical pulses because the instantaneous gain from the OPA temporally gates the seed pulses and restricts the generated incoherent fluorescence to a narrow time window. This allows the subsequent amplifiers, which are pumped by longer pulses, to operate at a lower gain, thereby generating less fluorescence and improving the temporal contrast [17]. After initial prototyping, front ends based on this concept have been deployed on the MTW and OMEGA EP lasers [18], and similar systems are being used in other laser facilities [19–23]. The UOPA deployed on MTW has a similar design and performance to the units deployed on OMEGA EP [18], as described in Fig. 7.

- A commercial mode-locked laser (GLX-200, Lumentum) provides seed pulses synchronized to the master reference clock doubled to 76 MHz at an average power of 200 mW. The 250 fs pulses (FWHM bandwidth equal to 6 nm at 1053 nm) are stretched to a few picoseconds by a two-grating stretcher for better temporal overlap with the pump pulse in the UOPA crystal.
- A diode-pumped Nd:YLF regenerative amplifier operating at 5 Hz amplifies one pulse from the 76 MHz train to ~0.5 mJ. Spectral gain narrowing reduces the bandwidth to 0.15 nm, which corresponds to a pulse duration of the order of 10 ps. This regenerative amplifier is similar to the one described in the previous Subsection 2.C, except for the compensation of self-phase modulation via intracavity-cascaded second-order nonlinearities [24]. That pulse is frequency-doubled with a 70% conversion efficiency and temporally synchronized with the seed pulse at the UOPA crystal. Coarse timing is performed

using the Vernier effect between cavity round-trip in the regenerative amplifier and the mode-locked laser, which are of the order of 13 ns but differ by approximately 300 ps. A remotely controlled fiber delay line with a range of 330 ps allows for fine delay tuning.

- Parametric amplification in a 5 mm BBO crystal yields signal pulses at the 10 μJ level.

The UOPA provides approximately four orders of magnitude energy amplification while restricting the associated parametric fluorescence to a few picoseconds around the output pulse [17]. This makes it possible to reduce the required gain in the OPCPA stages, where the pump pulse has a duration of a few nanoseconds and therefore significantly reduces the contrast degradation resulting from nanosecond fluorescence.

G. Offner Stretcher

The UOPA output pulse is stretched to ~1.8 ns (FWHM) in the Offner stretcher [25] with a dispersion of ~ − 300 ps/nm (positive second-order dispersion). Chirped-pulse-amplification systems traditionally use a static stretcher and set the pulse width by adjusting the compressor's parameters, such as the grating separation and incidence angle [26]. A static design was chosen for OMEGA EP's large-scale vacuum compressor, however, to minimize its optomechanical complexity; therefore, pulse-width adjustments must be performed using the Offner stretcher. The MTW, as the prototype front end for OMEGA EP, was used to develop this approach. After the MTW picosecond compressor is aligned in air, the vacuum chamber is closed, pumped down, and no further adjustments are made. All modifications for optimizing pulse compression for the shortest pulse or increasing it up to 200 ps are made using the Offner stretcher.

The stretcher (Fig. 8) uses a single-grating, double-pass geometry with a roof mirror (i.e., the beam diffracts four times off the
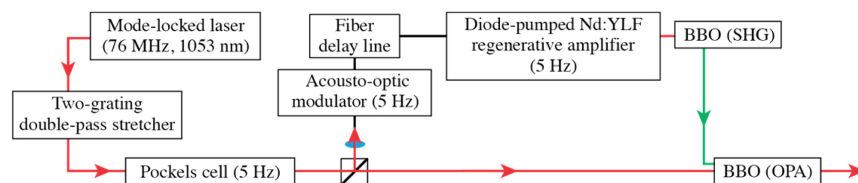

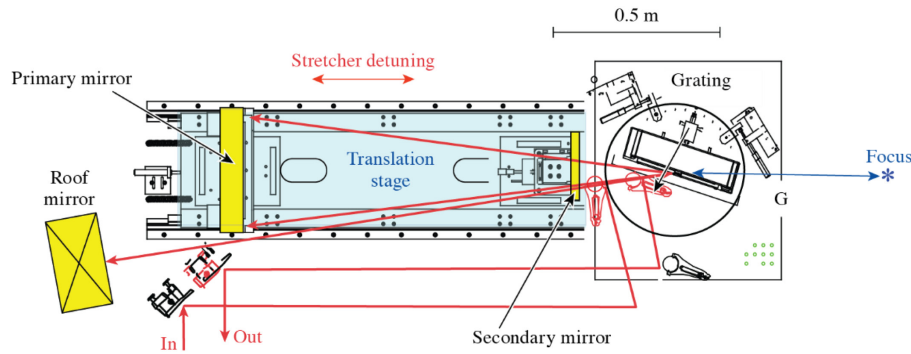**Fig. 7.**   Block diagram of the broadband front end.

Fig. 8. Stretcher setup. *G* is the distance between the common focus of the mirrors and the grating.

grating) [25]. The gold-coated grating (165 mm × 220 mm) has a line density of 1740 lines/mm. An image of the grating is formed with a negative slant distance using a spherical-mirror Offner telescope, as required to produce positive second-order dispersion that can be compensated by the grating compressor [27]. The telescope's concave primary and convex secondary mirrors are mounted on a single translation stage, allowing the telescope to be moved over the range of +200/ −150 mm from the best-compression position with micrometer accuracy to change the separation between the grating and its image. This changes the stretch ratio (SR) and, consequently, the compressed pulse duration, and either sign of chirp can be achieved (see also Section 3.C).

We measured the SR at different positions of the stretcher base with two pins installed in front of the secondary mirror of the stretcher to block portions of the spectrum. SR was determined from the separation of the notches induced on the measured pulse shape and spectrum, as shown in Fig. 9. The SR in units of ps/nm is calculated as

$$\mathrm{SR} = 2G \frac{\lambda d^2}{c * \cos^2 [\theta_\mathrm{d} (\omega_0)]},$$

where G is the distance between the grating and the focal spot of the primary mirror in the stretcher; d is the grating line density; $\theta_d (\omega_0)$ is the diffraction angle at the central frequency; and λ_0 is the central wavelength. The stretcher varies not only the pulse duration but also the sign of the chirp, which is critical for experiments in a gas jet, for example.

After the stretcher, a Pockels cell selects a single stretched pulse from the 76 MHz train if the UOPA stage is bypassed. Finally, a 2 m long telescope adjusts the beam size at the first OPCPA stage.

H. Optical Parametric Chirped-Pulse-Amplification Stages

OPCPA is a key aspect of the MTW laser in its broadband mode because it amplifies stretched pulses with more gain, larger bandwidth, and higher temporal contrast than would be possible with Nd-doped amplifiers alone [28]. It was built in two stages: a two-crystal preamplifier (PreAmp) provides high gain, while a single-crystal power amplifier (PowAmp) yields high energy-extraction efficiency. Operating the preamplifier with some OPCPA reconversion and the power amplifier in
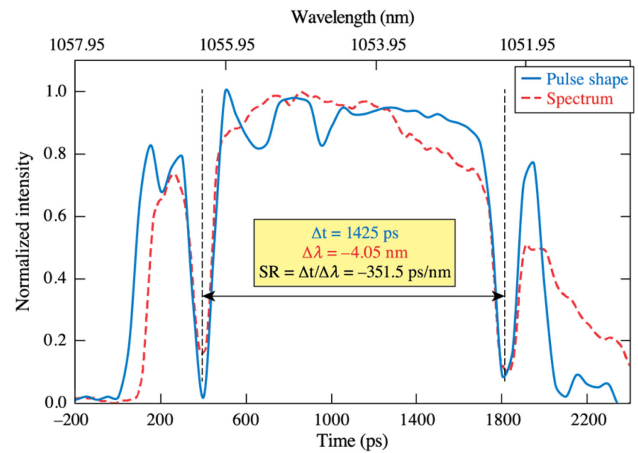

Fig. 9. Example of stretch ratio (SR) measurement.

saturation balances the effect of pump-energy variations while maximizing energy extraction [29].

LBO crystals were selected for PreAmp and PowAmp because of their broad angular acceptance and low pump-to-signal walk-off compared with those of other nonlinear crystals, such as BBO and KDP, commonly used in degenerate OPCPA systems at 1053 nm. The broad angular acceptance of LBO reduces the OPCPA system sensitivity to pump-laser wavefront errors, which can lead to reduced efficiency and undesirable beam modulation. Minimizing pump-to-signal walk-off also improves overall efficiency and beam quality, especially in a preamplifier based on long crystals and small beams.

The OPCPA amplifier setup is also shown in Fig. 5. After SHG of the CLARA beam, the Pellin–Broca prism separates the second-harmonic beam from the fundamental beam. Two dichroic mirrors dump the residual IR beam to prevent its propagation into the OPCPA stages and avoid nonlinear interaction with the pump beam. The half-wave plate (λ/2 #1) and the polarizer P1 distribute the pump energy at 527 nm between the PreAmp and PowAmp with an adjustable ratio of about 1:10. The other two wave plates and polarizers (λ/2 #2 with P2 and λ/2 #3 with P3) independently vary the pump energy in the preamplifier and power amplifier stages. The vacuum image relays VIR1 and VIR2 image the SHG crystal on the OPCPA crystals and set the pump FWHM beam size to 3 mm in the preamplifier and 6 mm in the power amplifier. The calorimeters K1 and K2 measure pump beam energies in the PreAmp

and PowAmp stages, K3 and K4 measure the residual pump energies, and K5 measures the output signal energy.

The seed beam is injected into the PreAmp under a slight noncollinear angle (8 mrad external) to the pump beam. A noncollinear regime between the pump and the seed beams in the phase-matching plane prevents self-doubling of the intense amplified signal and reduces pump-signal walk-off effects. That also simplifies separating the amplified signal beam from the residual pump and idler beams. The 15 ps (rms) temporal jitter between the pump and the seed lasers yields excellent wavelength stability of the amplified OPCPA signal. The PreAmp uses two 5×5 mm aperture LBO crystals, 29.75 and 36 mm long. The crystals are critically phase-matched in a walk-off-compensated arrangement for which the main optical axes of crystals are antiparallel.

Orientation of the crystals in the preamplifier is extremely important to prevent parasitic SHG [30], which reduces the output signal beam energy and shapes the output signal's spectrum. It is critical to set the axis of the second crystal at a larger angle with seed beam propagation than in the first crystal to suppress parasitic SHG of the OPCPA signal. The first crystal can be oriented in an antiparallel direction and matched with the SHG angle, but parasitic SHG is negligible there due to the low intensity of the OPCPA signal. Furthermore, both preamplifier crystals are tipped out of the phase-matching plane to avoid round-trip amplification of spontaneous parametric fluorescence that is reflected off the crystal faces. Referred to as optical parametric generation, this noncompressible incoherent pulse is seeded by vacuum noise and has a much larger divergence and broader spectrum than the coherent signal. While all crystals have antireflection (AR) coatings, even a small residual reflection from the crystals faces can be amplified due to the extremely high parametric gain. Multiple reflections and passes through the amplifier can decrease the gain experienced by the chirped signal, resulting in a step-like pulse shape and spectrum [31].

The PreAmp stage operates at a nominal pump intensity of $1 \, \text{GW/cm}^2$. The $3 \, \text{mm} \times 3 \, \text{mm}$ (FWHM) square pump beam is smaller than the round Gaussian seed beam (diameter ~ 4.5 mm at FWHM) from the stretcher. The high-gain parametric process reshapes the seed beam, making the output signal beam spatial profile close to that of the pump beam.

If the UOPA is bypassed, the seed pulse is amplified from 600 pJ to 30 mJ, corresponding to a net gain of 5×10^7 with a conversion efficiency exceeding 24% (Fig. 10). Separately, the pump depletion is measured by blocking and releasing the seed beam. This shows a value of 71%, which is in good agreement from the value calculated from the measured signal-to-pump conversion efficiency. Driving the OPCPA preamplifier slightly into the reconversion regime optimizes the two-stage system's efficiency as well as the energy stability [32]. With gain from the UOPA, the seed energy into the PreAmp is $\sim 8 \, \mu\text{J}$. It requires much less pump beam intensity to obtain an even better conversion efficiency of 27% (Fig. 10). The output signal energy with UOPA is only 15 mJ, but that reduction in energy is compensated at the following stages of amplification. Pumping the PreAmp at a lower intensity significantly reduces OPG and improves the pulse contrast after recompression (see Section 3.D).
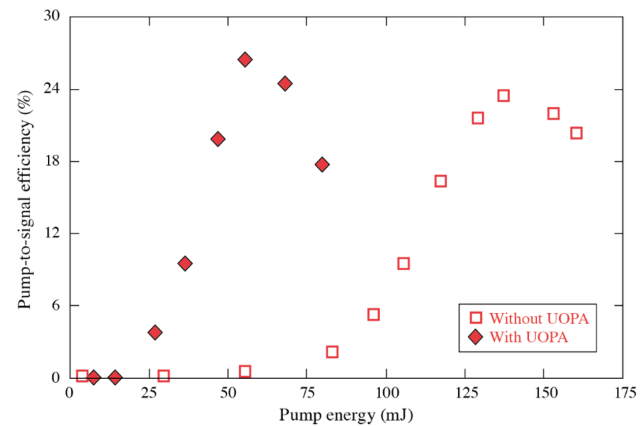

Fig. 10. PreAmp pump-to-signal conversion efficiency with (diamonds) and without (squares) the UOPA.

The PreAmp output signal beam is image-relayed with a magnification of about $2\times$ to the OPCPA PowAmp stage. Pump-pulse energies up to 640 mJ are delivered to a $10 \, \text{mm} \times 10 \, \text{mm} \times 16 \, \text{mm}$ LBO power-amplifier crystal. The pump intensity in the power amplifier exceeds that of the preamplifier by 20%–40%. This is possible without increasing the risk of damage because the PowAmp beam is $2\times$ larger and therefore has less modulation from diffraction effects at optics that are not at a pump-beam image plane. At the maximum pump energy, 265 mJ pulses have been measured at the output of the PowAmp, corresponding to 37% pump-to-signal conversion efficiency reached with no observed saturation. The total system efficiency, including preamplifier and power amplifier, is 34% with an energy stability of 1% (rms) over 100 shots.

The spatial reshaping of the seed is mostly due to the high-gain PreAmp, but the output signal spatial profile is strongly modulated because of the nonlinear dependence of the gain with respect to the pump intensity. In the PowAmp, the gain dependence on the pump energy is more favorable: low-intensity areas in the seed beam experience higher gain, whereas high-intensity areas reach saturation faster and therefore experience lower gain. This smooths the signal spatial profile, and the range of intensities across the beam is reduced with a peak-to-mean value of less than 20%. The amplified signal beam's near-field profile shown in Fig. 11(a) was measured with an 8 bit CCD camera. The corresponding spectrum is shown in Fig. 11(b).

I. Programmable Spatial Light Modulator

The OPCPA output beam is shaped by a PSLIM and amplified in the Nd:glass rod and disk amplifiers. PSLIM is a beam-shaping system consisting of a high-resolution spatial light modulator (Hamamatsu LCOS-SLM X10468) and a beam-shaping algorithm. The algorithm creates a high-frequency spatial-phase modulation on the PSLIM, where the depth of the modulation controls the amount of the zeroth-order diffraction that is transmitted [33,34]. The higher-order diffraction terms are lost outside the field of view of the system image relays. Additional phase correction, although limited to about one wave peak-to-valley, can be achieved by low-frequency modulation in the PSLIM. The PSLIM and RA with associated diagnostics are located on the rod amplifier table, as shown in
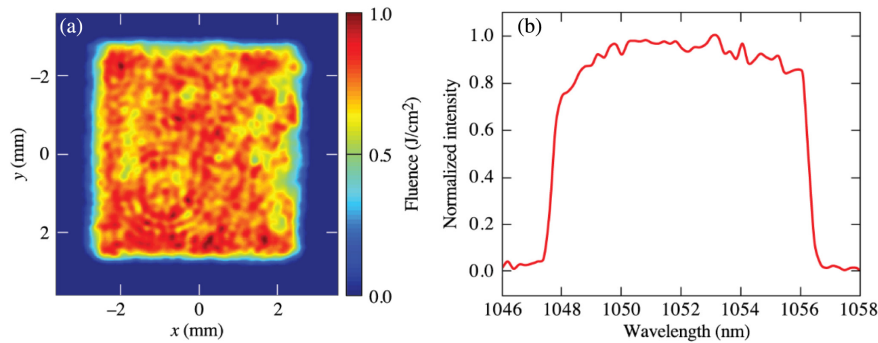
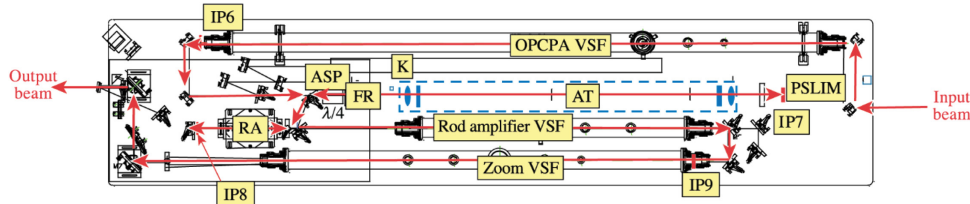**Fig. 11.**   (a) OPCPA output beam and (b) spectrum.

Fig. 12.   Table layout. VSF, vacuum spatial filter; IP, image plane; ASP, alignment sensor package; K, calorimeter; FR, faraday rotator; AT, anamorphic image relay telescope.

Fig. 12. The OPCPA output beam is up-collimated (2×) and spatially filtered in the OPCPA VSF. The PSLIM modulates the beam intensity and phase to correct the incoming beam and precompensate the RA gain nonuniformity. It is located in the middle line of the RA table, after the 20 mm ceramic Faraday rotator (FR) and the anamorphic image-relay telescope (AT), shown in Fig. 12 as the dashed box.

The FR and the half-wave plate protect upstream optics from backreflections. Due to the relatively low damage threshold of the PSLIM (230 mJ/cm² with 2.5 ns pulses at 5 Hz), an anamorphic telescope is used to image the PowerAmp on the spatial light modulator. It changes the square OPCPA beam profile (12.8 mm FWHM) to a rectangular profile [15.7 mm (H) × 11.8 mm (V)] that maximizes the use of the PSLIM aperture [16 mm (H) × 12 mm (V)] and reduces the average fluence on the device. The outer horizontal cylindrical lens pair images the horizontal dimension, whereas the inner pair images the vertical dimension independently. Another benefit of an anamorphic telescope is that it has separate focal lines between the lens pairs (horizontal and vertical) instead of the usual focal spot of a conventional telescope. As a result, the maximum intensity is below the air-ionization level, and a vacuum tube between the lenses is not necessary.

The PSLIM requires an exact and stable position of the beam on the modulator, which is set using an input alignment sensor package (ASP), and the energy is checked using an input energy calorimeter (K). The Shack–Hartmann wavefront sensor characterizes the phase at the output image plane of the rod amplifier. PSLIM can be bypassed, if necessary, by inserting a pair of mirrors in front of it. After PSLIM, the spatially modulated beam is polarization-switched using the FR to the RA.

J. Nd:Glass Rod Amplifier

The next stage of amplification is the two-pass rod amplifier. The amplifying medium is a 1 in. diameter, four flash-lamp-pumped, 240 mm long Nd:glass rod. The small-signal gain in the rod is significantly different for the broadband OPCPA signal (bandwidth of 8 nm) and for the narrowband signal from the Nd:YLF amplifiers because of its amplification bandwidth. While the narrowband gain reaches 85, the broadband gain does not exceed 70 [Fig. 13(a)] at the same RA voltage of 2.4 kV. In practice, lamps are fired at a voltage of 2.0 kV, corresponding to a narrowband small-signal gain of 40, in order to achieve a desired output energy with less distortion of the spatial beam profile.

The PSLIM plane is imaged to a flat folding mirror after the RA (Fig. 12). The quarter-wave plate ($\lambda/4$) in front of the RA produces circular polarization, increasing the safe level of energy inside the rod. It also rotates the linear polarization after two passes so that the thin-film polarizer passes the beam to the next vacuum spatial filter (RA VSF). The finite extinction of polarizers and wave plates can allow a cavity to form between the folding mirror behind the RA and the PSLIM, which can result in parasitic lasing. A slight intentional misalignment of the folding mirror introduces a small amount of walk-off per pass, which has little effect on the beam, but introduces enough loss for multiple passes to inhibit parasitic lasing. The gain nonuniformity of the RA can be precompensated by PSLIM. Figure 14(a) shows the profile of the RA output beam with bypassed PSLIM. Figure 14(b) shows that PSLIM can significantly improve the beam uniformity thanks to its closed-loop correction algorithm.

K. Main Nd:Glass Disk Amplifier

Upon exiting the RA, the pulse energy is up to ∼ 3 J. Before the beam is injected into the DA, it is expanded to 26 mm × 26 mm
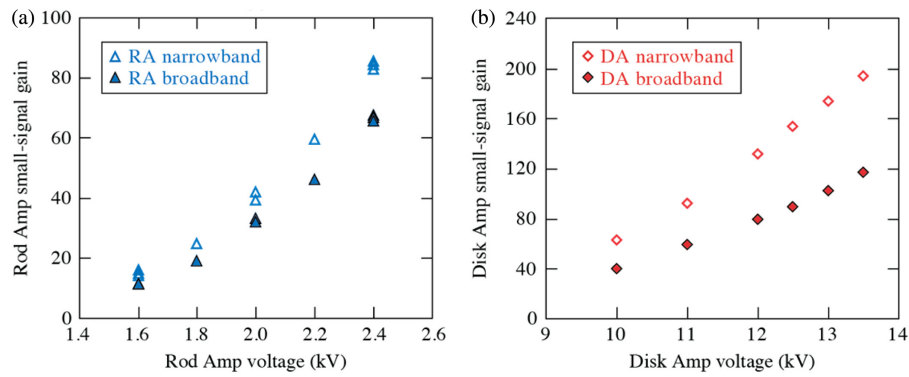
Fig. 13.   Small-signal gain of (a) the double-pass rod amplifier and (b) the four-pass disk amplifier for narrowband (open symbols) and broadband (solid symbols) signals.
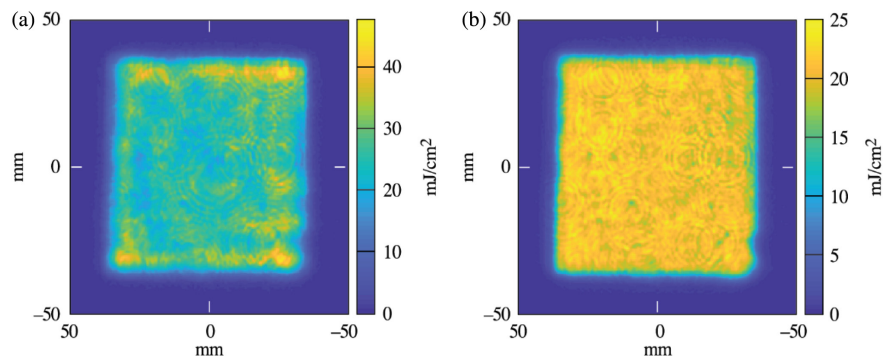

Fig. 14.   Rod amplifier beam profiles measured at the plane equivalent to the last hit of the beam on the grating in the compressor (a) without and (b) with PSLIM correction.

by a three-lens zoom telescope, which has the vacuum spatial filter between the first two lenses (Zoom VSF). The final stage of amplification is realized in a standard LLE-designed 15 cm diameter aperture DA, which consists of four Nd:glass (Hoya LH-8) disks mounted at the Brewster angle. It is powered by a power-conditioning unit capable of delivering up to 275 kJ when the 132 cm flash lamps are charged to the maximum voltage of 14.8 kV [35]. The peak current in each circuit is approximately 7 kA with a pulse width of 550 µs (FWHM). A pre-ionization and lamp check circuit allows for reliable operation even at reduced capacitor bank voltages. Ignitron vacuum tubes are used to switch the high voltage and current. Since flash-lamp pumping deposits a significant amount of heat in the amplifying Nd:glass disks, thermally induced changes in refractive index and thermal expansion can affect the beam profile and pointing of subsequent shots. For this reason, a 20 min delay between shots is enforced for 10 kV shots and 45 min for 13 kV shots.

The amplifier housing is shown in Fig. 15. The beam is folded in a four-pass geometry to maximize the amount of extracted energy, to use more space in the available aperture, and to maintain beam uniformity. Each pass occupies a different area of the disks. There is the 2× up-collimation telescope (DA VSF) between the second and the third pass. The cross-section of the 15 cm diameter aperture of the DAt with the numbers and orientations of passes is also shown in Fig. 15. A 45 mm diameter Faraday isolator is located between the second and the third pass to protect the laser from backreflections. Mirrors between

the passes rotate the beam up–down, left–right, and by 90° to minimize the impact of any gain nonuniformity across the disks.

Although the flash lamps may be fired at voltages as high as 14.8 kV, the maximum used in operations is 13.5 kV, and they are usually operated at 10 kV to lengthen their lifetimes. Under these conditions, the small-signal gain from a single pass is ∼ 3. After four passes through the amplifier, the final energy of the laser is >120 J. In general, the RA and DA voltages are kept at modest levels (2 and 10 kV, respectively) to maintain the same time between shots and to minimize thermal effects. Two half-wave plate/polarizer throttles between the OPCPA stages and the RA can be used to control the MTW output energy if necessary. Similar to the RA, the DA is also limited in spectral gain and has a higher small-signal gain for a narrowband input signal than for a broadband one [Fig. 13(b)].

L. Backreflection Protection

After the DA, the kinematic switchyard, SY3, directs the beam to pump in the last stage of the all-OPCPA laser or to be recompressed in the picosecond vacuum grating compressor chamber (ps-GCC). The all-OPCPA arm includes an SHG stage and is therefore free from any risks of a backreflected beam; however, the GCC path must be protected from a target reflection. Measurements from our backreflection diagnostic show that the energy reflected from a target is sensitive to target size, material, and the angle of incidence. The fraction of reflected energy can be as high as 8%. Without a protection system, backreflections
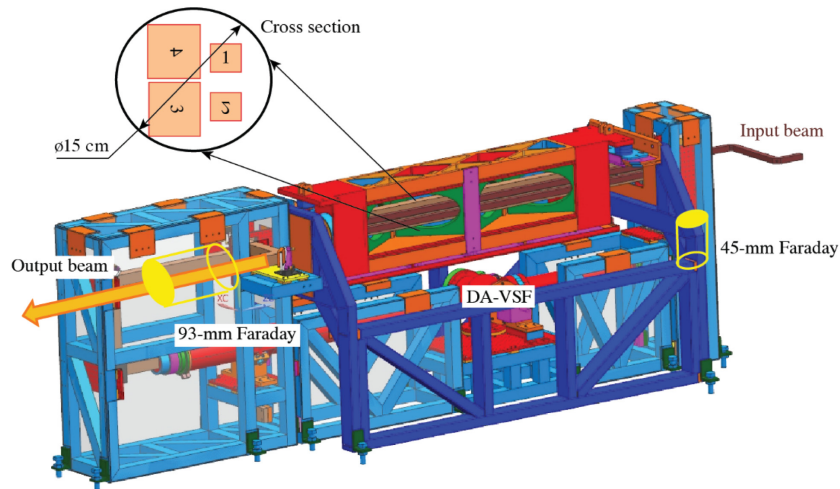
Fig. 15. Disk amplifier structure. Pass numbers (1–4) showing beam rotations.

could reach the DA and RA, which still have high gain, and cause catastrophic damages to front-end optical elements. Four Faraday isolators are used between the master oscillator and the target chambers. The last and largest Faraday rotator (Passat) with an extension ratio of >20 dB contains two 93 mm diameter terbium glass disks. It has a damage threshold of 2 J/cm^2 for nanosecond pulses and limits the operation energy to 50 J. The large-aperture liquid crystal wave plate and polarizer have higher damage thresholds and do not limit the maximum system output energy.

M. Picosecond Grating Compressor Chamber

The compressor is built in a two-pass scheme with a roof mirror between passes. Both gratings are dielectric with 1740 lines/mm. The first grating with size 220 × 165 mm is called G1/G4 to follow the traditional terminology of four-grating compressors and identify each hit of the beam on the grating. The second grating, G2/G3, is 350 × 190 mm. The G1/G4 grating is mounted on a rotation stage, while G2/G3 has both rotation and translation stages. The compressor is located inside the vacuum chamber (Fig. 16). The input beam (red path) of 70 mm × 70 mm (FWHM) enters the compressor chamber through port P1 and after the turning mirror M1 hits the upper G1 area of the grating G1/G4. The diffracting beam goes to the G2 area of the grating G2/G3 and then after the roof mirror RM comes back to G1/G4. The leaky mirror LM1 transmits about 1.5% of the output beam to the compressor diagnostics package (CDP) through the port P2.

The recompressed pulse can be directed to different ports for different applications. Through the vacuum port P3, the output beam (blue path) goes to the STC. The turning mirror M2 on a translation stage directs the beam into the UDP chamber (green path) through the vacuum port P4 or into the CTC through the window port P5 (yellow path). The CTC chamber is separated from the GCC by a lens or a window to enable target experiments at other vacuum levels. The window port P6 passes the main output beam (orange path) on the CDP table for low-intensity experiments and/or diagnostics. Viewports P7
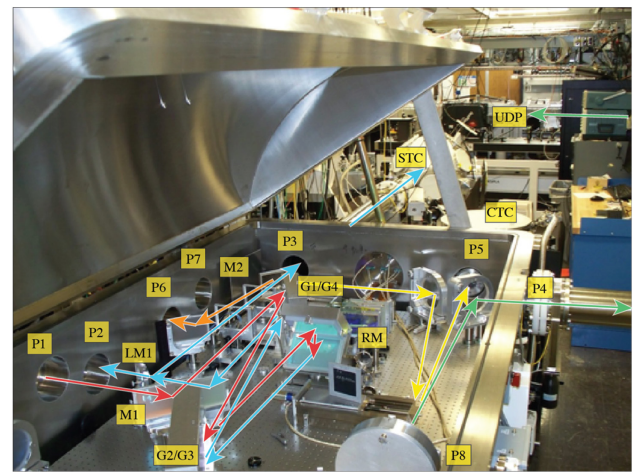

Fig. 16. Picosecond grating compressor chamber (ps-GCC). P, port; M, mirror; LM, leaky mirror; RM, roof mirror; G1/G4, the first grating; G2/G3, the second grating; STS, spherical target chamber; CTS, cylindrical target chamber; UDP, underdense plasma chamber.

and P8 are used for visual inspection of the gratings. All optical ports P use standard NW160 flanges. The chamber also has four facility NW250 ports for vacuum pumps, controls, and electrical feedthroughs.

The ps-GCC optics are mounted on a honeycomb breadboard (8 ft × 4 ft) with six support legs that are mechanically decoupled from the compressor chamber body using vacuum bellows. The stainless-steel compressor chamber, weighing ~6 tons, is supported by four separate legs. The NW250 vacuum port is located beneath the chamber. The compressor chamber is not specified for ultrahigh vacuum; therefore, it has Vinton O-rings for sealing and does not have baking equipment. The best vacuum with a turbo pump is 2 × 10^{-6} Torr. Better vacuum levels (3 × 10^{-7} Torr) have been achieved with a cryogenic pump, but some experiments and measurements are sensitive to its additional vibration.

N. Harmonics Generation

Some experiments on MTW require optical pulses at central wavelengths different from 1053 nm. For example, picosecond time-resolved measurements of dense plasma line shifts [36] require the second harmonic at 526.5 nm. Timing calibration of x-ray streak cameras requires short subpicosecond pulses in the deep-UV region. To satisfy these requirements and to increase the temporal contrast of the compressed pulses [37], the MTW output beam can be converted into the second or fourth harmonics. Several sets of large-aperture KDP and DKDP crystals (up to 85 mm × 85 mm) are available for use, depending on the required pulse energy and duration. The maximum measured SHG conversion efficiency of 80% for a subpicosecond pulse was obtained in a 2 mm thick KDP crystal. Fifth-harmonic generation (5HG) is necessary for many plasma diagnostics [38,39]. To investigate and optimize 5HG, after four round-trips, the CLARA beam is picked up by the switchyards SY1 and SY2 on an RA table and sent to the 5ω table (see Fig. 3).

O. MTW Configuration to Pump an All-OPCPA Laser

The MTW laser can be configured in narrowband mode to pump the last amplifier of an all-OPCPA laser system (9.5 J, 19 fs pulses) [10,40]. This system is designed to deliver compressed 0.5 PW pulses to the UDP chamber. For this application, the MTW broadband front-end (the master oscillator, UOPA, stretcher) and OPCPA stages are not used. Instead, the narrowband CLARA beam is steered using SY1 before it is frequency-doubled in the SHG section (Fig. 3). Three round-trips in the CLARA provide a 300 mJ, 1.6 ns pulse. The beam is injected back into the main path by SY2 after the transport vacuum image relay before PSLIM. Up to 150 mJ can be used if PSLIM is not bypassed due to its damage threshold.

After the RA and the DA, SY3 steers the beam to the SHG table. Because SY3 is located before the 93 mm Faraday isolator, the output energy is not limited to 50 J by the damage threshold of the Faraday isolator; therefore, up to 105 J can be provided. A VSF reduces the beam size to 44 mm × 44 mm and images the beam into a second-harmonic crystal (DKDP, 65 mm × 65 mm × 17 mm), where the pulse is frequency-doubled with an efficiency as high as 76%.

Two periscope towers transport the MTW beam to a neighboring laboratory where the all-OPCPA system is located (see Fig. 3). The ultrabroadband front end generates seed pulses centered at 920 nm with 140 nm of bandwidth, after stretching to 1.3 ns. The MTW pump beam is overlapped in space and time with the seed beam in the NOPA5 crystal, a 63 mm × 63 mm aperture, 52 mm long DKDP crystal, which has a 70% deuteration level. For the first test runs, up to 40 J of pump energy was used, which was converted into a signal beam with efficiency as high as 40%, which corresponds to 12 J. Sub-20 fs pulses were measured after a femtosecond compressor, which has 75% transmission.

P. Target Chambers

Currently MTW has three target chambers: STC, CTC, and UDP (Fig. 3):

– The STC is a 90 cm diameter stainless-steel sphere and is connected to the ps compressor by a vacuum tube ~3 m long. It contains a steering mirror, an off-axis parabola (OAP) at ω or 2ω and a five-axis target manipulator.

– The CTC is a 46 cm diameter cylinder and has a 75 mm diameter window between the GCC and CTC. This window allows for experiments to occur at different pressures between the CTC and GCC and also protects the GCC from possible contamination from CTC targets. The 100 in. focal length mirror inside the GCC focuses the MTW beam into the CTC.

– The UDP chamber is separated from the GCC by 10 m of vacuum beam path with several beam steering mirrors and an alignment sensor package. It is rectangular with approximately 114 in. × 60 in. of breadboard space available for experiments. It can be run with up to 21 ports for diagnostic access to the experiments and is surrounded by diagnostics tables. The chamber supports both gas-jet and gas-cell targets for underdense plasma experiments. The targets can be ionized and preheated using the Underdense Plasma-Ekspla (UDP-E) laser system. UDP-E is a 1.5 ns FWHM heater beam, which can be configured to run at 10 J (1ω), 8 J (2ω), or 5 J (4ω). The final focusing geometry of MTW is reconfigurable. The laser beam is currently focused using a 1215 mm focal length singlet.

3. DIAGNOSTICS AND LASER PERFORMANCE

A. Compressor Diagnostic Package

Every stage of MTW has multiple diagnostics, but the compressor diagnostics package (CDP) is the most critical. It measures MTW parameters under high-energy conditions and provides output beam characteristics that are necessary for target shots and other experiments. It is shown in Fig. 17 and consists of the GCC input beam (long-pulse) diagnostics in red and GCC output beam (short-pulse) diagnostics in blue.

The amplified beam from the DA comes to the CDP table through a VSF with a magnification of 1.45×. The first input diagnostic is the "fourth" grating-equivalent near-field camera G4E, located behind the leaky mirror LM3. It measures the beam near-field profile at a plane equivalent to that of G4, i.e., the grating surface on which the pulse is the shortest before leaving the compressor. Before a full-energy shot campaign, the GCC input is blocked using either a turning mirror (M2) and calorimeter (Cal 1) or a beam dump, and the beam profile is measured on a high-energy shot using G4E. Beam-modulation analysis is performed to establish safe-operation limits for propagation in the compressor. The allowed level of beam modulation depends on the required energy and compressed pulse duration; for the highest energy and shortest pulse, the modulation must be below 20% peak-to-mean to protect the gratings.

The input alignment sensor package (ASP IN) is located behind the leaky mirror (LM2) and consists of pointing and centering cameras, which are used to align mirrors M1 and LM3, respectively. The far-field camera (FF) is necessary to control the alignment of the last leaky mirror LM2 before GCC. A corner cube installed in front of the GCC in combination with a quasi-cw or low-energy OPCPA beam is used to check the alignment. The residual beam after the ASP IN's wedge is
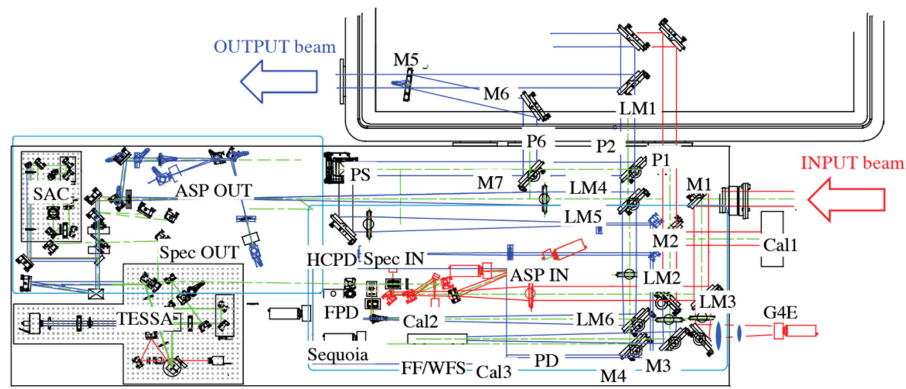
Fig. 17. Compressor diagnostic package, showing the diagnostics for the input beam (paths represented with a red line) and for the output beam (paths represented with a blue line). M, mirror; LM, leaky mirror; P, port; Cal, calorimeter; Spec, spectrometer; PD, photodiode; HCPD, high-contrast photodiode; FPD, fast photodiode; FF, far-field camera; ASP, alignment spatial package; WFS, wavefront sensor; PS, periscope; G4E, grating 4 equivalent; TESSA, time-expanded single-shot autocorrelator; SAC, scanning autocorrelator.

measured by the pickoff energy meter (Cal 2), which consists of an integrating sphere, a single-mode fiber, and a commercial picojoule–nanojoule scale calorimeter (Ophir PD10). The pickoff energy meter (Cal 2) is cross-calibrated to a 9 in. diameter full-energy calorimeter (Cal 1), which is an LLE designed and fabricated calorimeter. This calorimeter is based on temperature measurements of an absorbing glass. Similar calorimeters have been used on the OMEGA laser for many years for energies up to 1 kJ. The cross-calibration factor between Cal 1 and Cal 2 is relatively stable. It is measured at least every six months or after changes to the system that could affect it.

After the energy pickoff system, the beam reaches the input spectrometer (Spec IN). This is a Czerny–Turner spectrometer (Acton, SP-500), and the beam is coupled onto the spectrometer slit using a polarizing (PZ) fiber.

The compressor output diagnostic package is more complicated. The main output beam is sent by the leaky mirror (LM1) toward a target chamber, while ~1.5% of the beam energy is transmitted through it and leaves the GCC through the vacuum port (P2). Several 4 in. × 6 in. mirrors split the output diagnostics beam into the high-contrast diagnostics line (LM4), the output ASP, the scanning autocorrelator (SAC), the time-expanded single-shot autocorrelator (TESSA), similar to [41], the output spectrometer Spec OUT line (LM5), the fast photodiode FPD line (LM6), and the synchronization photodiode PD line (M4).

The high-contrast diagnostics (HCD) are located on the upper level of the CDP, where the beam is delivered by the leaky mirror (LM4) and the periscope (PS) for low-energy on-shot diagnostics, or by the mirrors M5 and M6 and the mirror M7 on a kinematic base through port P6 for full-energy diagnostic when the main output beam is used only for diagnostics. The temporal contrast of the MTW laser in short-pulse operation has been characterized with a nonlinear scanning cross-correlator (Sequoia, Amplitude Technologies) and a high-contrast photodiode (HCPD).

Finally, the backreflection monitor is located behind mirror LM2 in the backward-propagating direction. The leaky portion of the retro beam, coming from a target and transmitting through LM2, is measured by the calorimeter Cal3 (Laser Probe RjP 735). Alternatively, the path can be used to measure the wavefront of the MTW beam with a wavefront sensor (WFS). For that measurement, an additional flat mirror is installed in any position between LM2 and OAP before a target. A probe laser was used to calibrate the down-collimation optics in the wavefront measurement channel (not shown in Fig. 17).

B. Output Energy

The on-shot MTW output energy is measured using pickoff calorimeters cross-calibrated with a large-aperture calorimeter that covers a large energy range (1.5–1000 J). The pickoff calorimeters are located behind the leaky mirror on the CDP table, on the RA table, the SHG table, and the NOPA5 table; they are used to monitor losses through the system and the gain of the amplifiers. Figure 18 demonstrates the MTW energy map at different voltages for the RA and DA. Curves show the increase in output energy versus RA input energy for different RA and DA voltages. Each point has a shot number, energy density, and peak-to-mean beam modulation.

The pulse being recompressed in the GCC has two main energy limitations coming from the Faraday isolator and the gratings in the compressor. The limit of 50 J is set by the damage threshold of the terbium-doped glass ($2 \, \text{J/cm}^2$). The energy range below 50 J is shown in Fig. 18 as the safe zone (no shading). Because the Faraday isolator is located before the compressor, this limit does not depend on the recompressed pulse duration. The second energy limitation is set by the damage threshold of the compressor gratings, where the last hit on G1/G4 dominates. This limit does depend on the pulse duration; for example, at 10 ps, the measured damage threshold is $1.7 \, \text{J/cm}^2$, which corresponds to the limit of output energy of 85 J. In practice, safe operation must also consider beam modulation and a safety factor of 20%, which results in maximum energy on the final grating of approximately 70 J. The zone between 50 and 70 J is the moderate-risk zone (blue shading). The high-risk zone (pink shading) corresponds to energies above 70 J. The energy on target for a 10 ps pulse is typically kept below 36 J and below 18 J for the best compression at 500 fs.
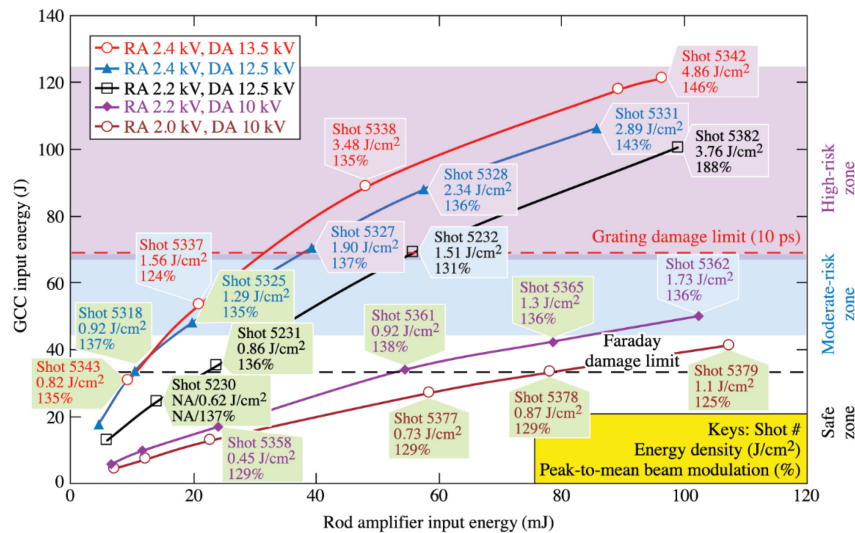
Fig. 18. MTW output energy for a range of RA input energies and operating voltages for the rod and disk amplifiers. Also shown are the damage limits imposed by the final Faraday isolator and the gratings for 10 ps pulses.

The maximum energy produced by MTW in narrowband mode is 120 J. This is acceptable for the all-OPCPA beam path because SY3 (Fig. 3) picks the full energy beam before the last Faraday isolator. The MTW beam in this mode is frequency-doubled to 2ω, and there is no risk of backreflections toward the MTW Nd:glass amplifiers at the fundamental frequency. Usually, we don't provide shots within high-risk and moderate-risk zones because it is dangerous for the laser. On another hand, all points on Fig. 18 correspond to real shots and demonstrate the full range of MTW shots energy, which would be safely available with compromising limitation factors. Planned upgrades to allow for MTW short-pulse operation at higher energies include the replacement of terbium-doped glass in the Faraday isolator with terbium gallium garnet (TGG) ceramic, which has a higher damage threshold of 5 J/cm^2, as well as the development and procurement of diffraction gratings with a higher damage threshold.

C. Pulse Duration

As mentioned above, the stretcher controls the pulse duration and the sign of the chirp. Covering the full range of pulse durations with a single diagnostic is not possible; therefore, several diagnostics are necessary and available to provide the required resolution and pulse-width range for any series of shots. A second-order scanning autocorrelator (SAC) is routinely used with the 5 Hz OPCPA beam prior to full-energy shots to measure the pulse autocorrelation. It covers a temporal range of 100 ps and is sensitive enough to align the compressor when required, which is rare. An autocorrelation trace of the shortest pulse is shown in Fig. 19(a) and has an FWHM of 497 fs, which corresponds to a pulse duration of ~369 fs. It is shown along with a simulated autocorrelation function calculated for a transform-limited pulse based on the OPCPA's output spectrum. Both autocorrelation traces overlap well with only a 4.8% mismatch between the FWHMs. A pedestal is observed in the autocorrelation traces measured for amplified and unamplified pulses, which match over more than three orders of magnitude.

It is attributed to spectral phase errors in the stretcher and compressor that often arise in chirped-pulse-amplification systems with large stretching and compression ratios.

TESSA, a single-shot autocorrelator, is required to measure picosecond pulses in a single shot, e.g., when the Nd:glass amplifiers are used. It has a temporal range of 40 ps set by the clear aperture of the noncollinear autocorrelation crystal (KDP, Type I, 10 mm). Figure 19(b) shows a typical series of single-shot autocorrelation traces, which demonstrates highly stable operation of the MTW laser. For this series, the stretcher was detuned away from best compression to provide higher energies on target.

To measure relatively long compressed pulses, a high-bandwidth 55 GHz photodiode (DSC10ER-39, Discovery Semiconductors) and 45 GHz oscilloscope (WaveMaster, Lecroy) are used. The duration of the resulting impulse response at 1053 nm is 17 ps, which overlaps with short compressed pulse diagnostics based on second-order autocorrelations. The real-time oscilloscope allows for single-shot acquisition; therefore, the diagnostic can be used on high-energy shots.

The gain narrowing in the RA and the DA modifies the spectrum of the MTW beam. The changes on the spectrum and, therefore, on the recompressed pulse duration depend on the voltage from each amplifier and OPCPA output energy. Figure 20 shows typical spectra and the corresponding pulses for different amplification stages when the stretcher is significantly detuned from its best-compression position.

Figure 21 shows pulse durations after the compressor measured with different diagnostics, depending on the stretcher translation stage position referenced to its position for best compression.

D. Temporal Contrast

The nonlinear cross-correlator provides contrast information with high temporal resolution over a ~200 ps temporal window [Fig. 22(a)], but its use is restricted to the OPCPA operating at 5 Hz. The high-contrast photodiode provides single-shot
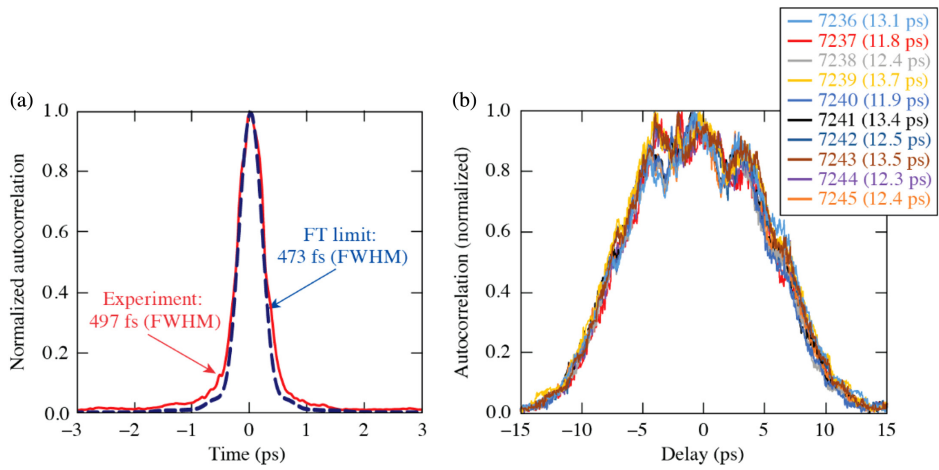
Fig. 19. (a) Measured best-compression autocorrelation function and the simulated autocorrelation function calculated for a transform-limited pulse based on the OPCPA's output spectrum. (b) Single-shot autocorrelation traces taken by TESSA in a series of full-energy, not best compression MTW shots.
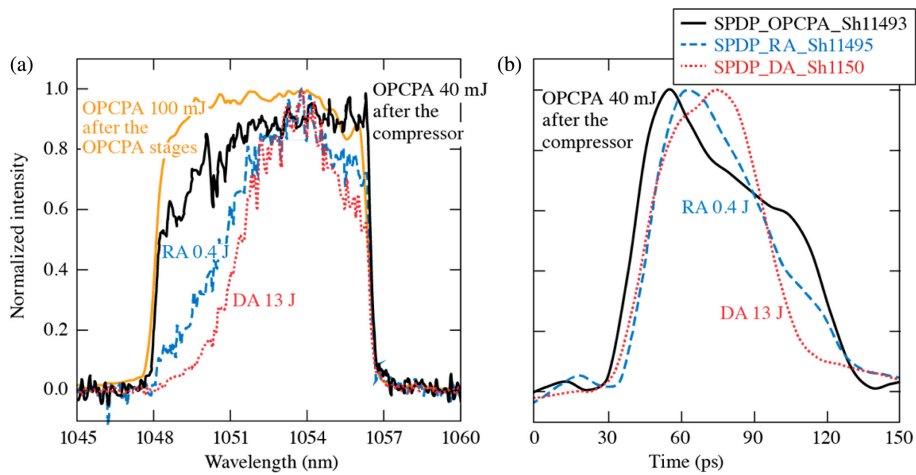

Fig. 20. (a) Output spectrum and (b) corresponding compressed pulse in different amplification regimes. The images are mirror symmetric due to positive residual chirp (longer wavelength in front) after recompression.
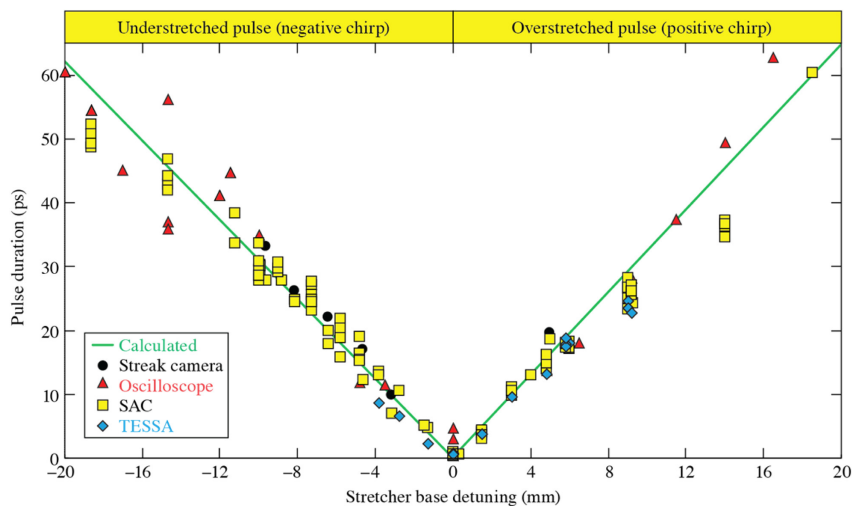

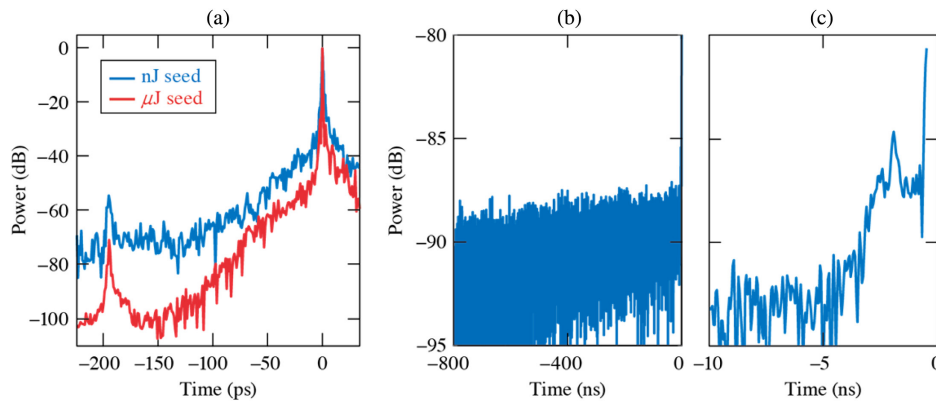**Fig. 21.** Compressed pulse duration adjustment by the stretcher.

Fig. 22. Temporal contrast of the compressed MTW pulse measured with (a) the nonlinear cross-correlator and (b), (c) with a photodiode and oscilloscope. In (a), the temporal contrast is shown before (nJ seed) and after (μJ seed) UOPA deployment.

contrast information over a much larger temporal window with resolution limited by the bandwidth of the photodetector and oscilloscope, approximately 200 ps [Figs. 22(b) and 22(c)].

Various experimental campaigns and analytical investigations have made it possible to identify the following prepulse contrast degradation features in front of the main pulse at $t = 0$:

- Laser fluorescence in the rod and disk amplifier is the main limitation up to a few nanoseconds before the main pulse. That fluorescence is generated over a long time window by stimulated emission.
- Parametric fluorescence from the OPCPA stages is the main limitation from a few nanoseconds before the main pulse to ~ -150 ps. That fluorescence is only generated over the 2.8 ns pump pulse but is stretched in the MTW compressor because it is spectrally incoherent. The deployment of the UOPA system led to a $\sim 300 \times$ reduction in the power level of the fluorescence, bringing its level down to ~ 95 dB, below the peak of the main pulse at best compression (duration ~ 385 fs). This contrast improvement is smaller than what is expected from the $\sim 10^4$ UOPA gain. The contrast limitation is thought to be caused by scattered residual 1ω narrowband light from the OPCPA pump laser that becomes amplified in the high-gain OPCPA stages alongside the chirped broadband seed but does not get recompressed, leading to a nanosecond pedestal.
- A pedestal around the main pulse is the main limitation from ~ -150 to -10 ps, a range over which its power increases by five orders of magnitude. High-frequency spectral phase modulations resulting from the spatial quality of optical components used where the optical spectrum is spatially dispersed, e.g., the grating-based stretcher [42,43], and high-frequency spectral amplitude modulation resulting from pump noise in the OPCPA stages [44–46] can induce such a pedestal. It is not clear which feature currently limits the temporal contrast of the MTW laser, but experimental campaigns studying the impact of narrow spectral filtering in the OPCPA pump laser using a volume Bragg grating showed that such filtering did not significantly improve the temporal contrast, although it was efficient at preserving the temporal contrast when the pump noise is purposely increased [47].

- A few discrete low-energy prepulses have been observed, in particular at -200 ps [Fig. 22(a)] and at -0.5 ns [Fig. 22(c)]. The origin of these prepulses is not known.

Detailed information on the contrast of the OMEGA EP laser, temporal diagnostics, and various contrast-degradation mechanisms can be found in other published works [18,48].

E. Focal Spot

The focal spot at the output of MTW is measured at the focus of the STC f/2 OAP using a 12 bit camera and a $10\times$ microscope objective. Attenuation of 10^6 is achieved using two 0.1% leaky wedged mirrors installed in an "antiparallel" configuration inside the GCC. Additional attenuation is provided using neutral-density filters. A typical focal spot is shown in Fig. 23(a) and has a slightly elliptical shape with major and minor axes widths of 6 and 5 μm, respectively. 85% of the energy is contained in a circle with a 5 μm radius [Fig. 23(b)].

F. Wavefront

The MTW wavefront is measured by a wavefront sensor WFS (see Fig. 17) installed behind the leaky mirror LM2 in the backward direction. This measurement requires careful calibration of noncommon-path wavefront aberrations in the diagnostic path and a determination of the single-pass contribution through the compressor. First, a flat mirror is installed at the GCC input, and a cw probe laser with a 50% splitter in front of the WFS calibrates the down-collimator, while the MTW beam is blocked. Next, the flat mirror is moved right before the OAP, and the wavefront of the probe beam is measured for two passes of the GCC. For a single pass, the wavefront error is only 0.075λ (p–v) over the full beam aperture. Finally, the wavefront of the MTW beam is measured for a double-pass through the GCC by the same wavefront sensor. A typical MTW wavefront for a single pass through the GCC is shown in Fig. 24 and has a p-to-v variation of 0.15λ over 98% of the MTW beam.
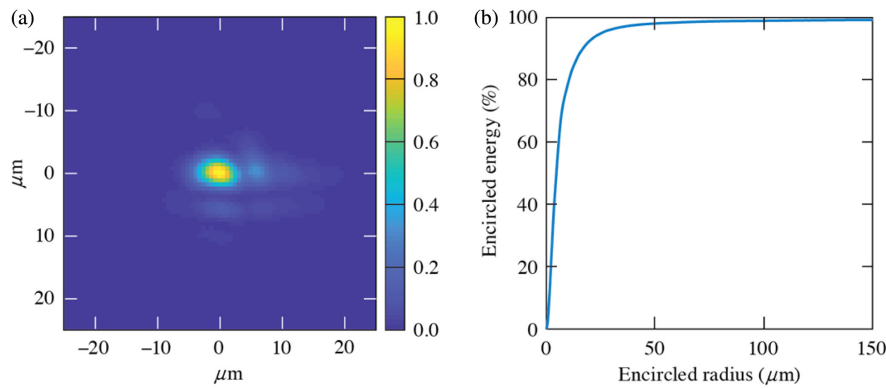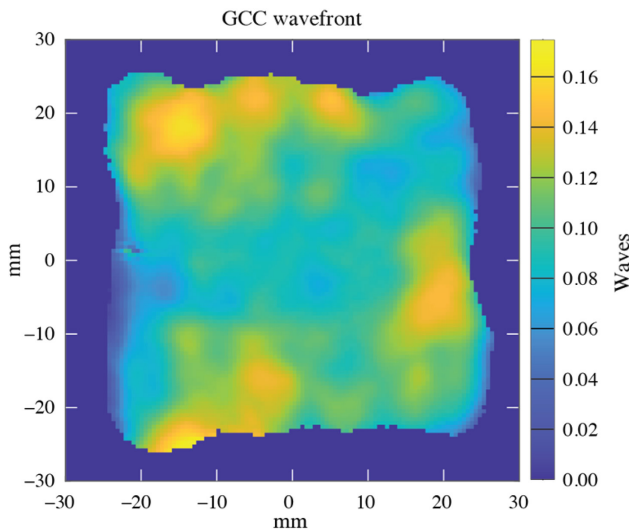
Fig. 23.   Focal spot of an MTW beam.

Fig. 24.   MTW output wavefront, with a 0.15λ peak-to-valley modulation.

4. MAIN APPLICATIONS AND RESULTS

A. High-Energy-Density Science

Relativistic (or "hot") electron beams provide a powerful source for heating matter to extreme energy densities in the Mbar to Gbar range [49]. One method for generating hot electrons is through high-intensity laser-matter interactions at focused intensities above 10^{18} W/cm^2 [50]. In these conditions, hot electrons are generated and deposit energy inside matter over picosecond time scales [51]. Understanding how hot-electron beams are generated and how they couple their energy to high-density matter is strongly motivated by a wide range of applications in high-energy-density (HED) science, including high-energy particle acceleration [52], material heating [53], x-ray source generation [54], plasma opacity [55], and laboratory astrophysics [56]. Of particular interest to the HED physics community is an improved understanding of the hot-electron source and material response to heating. For over a decade, the MTW laser has provided a flexible and diagnostic-rich platform to test the physics of intense radiation-matter interactions, hot-electron beam generation, and the radiative and hydrodynamic response of HED materials to ultrafast hot-electron energy deposition.

Early studies focused on the development of techniques for inferring the intense-energy coupling efficiency to hot electrons η_{L-e} in solid-target interactions [57–59]. This included the development of hot-electron confinement techniques for inferring η_{L-e} [60], the scaling of η_{L-e} with laser-pulse duration and intensity [61,62], and a determination of the time scale for hot-electron energy deposition inside solid targets [51,63]. These data provided a basis for understanding how to scale hot-electron generation to high-power, kilojoule-class laser-solid interactions on the OMEGA EP laser system [61]. Hot-electron generation and transport physics were studied on MTW using coherent transition radiation, revealing the role of magnetic collimation [64,65]. Novel hot-electron confinement geometries were developed based on small-mass targets for the creation of warm and hot dense matter [66]. Time-integrated and time-resolved plasma spectroscopies were developed [67,68] to diagnose the extreme states of matter that are generated and to test high-density atomic physics and energy-transport models [36,69], including the energy transfer dynamics in strongly inhomogeneous hot-dense-matter systems [70].

B. X-ray Spectrometers

A number of time-integrated and time-resolved x-ray spectrometers have been developed for the MTW setup, spanning the photon energy range from ~60 eV to ~30 keV. A suite of extreme ultraviolet (EUV) spectrometers, both time-integrated and time-resolved [67], measures the emission between 60 and 250 eV, with a spectral resolution of $E/\Delta E \sim 100$ and a temporal resolution of ~2 ps. Higher photon energies around 1 keV are covered by a time-integrated spectrometer (spectral range between 800 and 2100 eV and resolving power of $E/\Delta E \sim 450$) and a time-resolved spectrometer (spectral range from 1300 to 1700 eV, resolution of $E/\Delta E \sim 650$, temporal resolution of ~2 ps) [68]. X-rays with photon energies of ~8 keV are recorded in time-integrated mode with a flat highly oriented pyrolytic graphite spectrometer with a spectral resolution of $E/\Delta E \sim 700$, as described in [71], and time-resolved with an elliptical highly annealed pyrolytic graphite crystal spectrometer coupled to a ~2 ps streak camera [51]. A low-resolution survey spectrometer based on the single-photon-counting principle [72] covers a large energy range from ~5

to 30 keV with modest spectral resolution of $E/\Delta E \sim 40$ at 8 keV.

C. Neutron Diagnostics Development

In inertial confinement fusion (ICF) experiments on OMEGA, the neutron production width is an important metric used to assess the quality of such implosions. For accurate measurements, the impulse response of the neutron temporal diagnostic (NTD) [73] system, which records the neutron production width, must be known precisely. The NTD uses a plastic scintillator that converts neutron energy into light, which is time-resolved by an optical streak camera. A NTD system was designed and built for the MTW laser in order to develop techniques to optimize its impulse response. Figure 25(a) illustrates the experimental setup of the MTW-NTD system and the optical relay path from the target chamber to the streak camera. The optical relay path is composed of a scintillator, housed in the nose cone, a lens barrel, two mirrors, a filter, a focus lens, and an optical streak camera. An x-ray pulse is generated by the interaction of the tightly focused short laser pulse with the target material. These x-rays are converted into light by a BC-422 plastic scintillator, simulating the response to the neutrons produced in ICF experiments.

Figure 25(b) shows the CCD image from the optical streak camera for a MTW target shot. A 2 GHz optical time reference shown at the top of the image is used to calibrate the time axis. Reflections in the optical path cause an external signal outside the nominal image of the scintillator. Since the scintillator has a long decay constant of ~1.2 ns, the information about the width of the x-ray emission is encoded in the rising edge of the signal. A special deconvolution procedure has been developed to extract the temporal history of the emission from the streak camera image [73]. A number of optimizations in the optical path, the target material, and laser conditions were required to extract the intrinsic impulse response of the NTD setup, which was measured to be 22 ± 2 ps.

D. Flying Focus

Several experiments have been conducted to validate the "flying focus" concept, where the combination of temporal chirp and longitudinal chromatic aberration provides unprecedented spatiotemporal control over the velocity of a high-intensity focal spot over distances far exceeding the Rayleigh length [74,75]. The flying focus is expected to benefit several applications ranging from Raman amplification [76,77] to photon acceleration [78] and laser wake-field acceleration [79]. In the experiments, the stretcher was tuned to deliver prescribed linear chirps, positive or negative, ranging from tens to hundreds of picoseconds. The beam was then focused using a diffractive lens to create an extended focal region in which the constituent colors within the MTW bandwidth were dispersed linearly along the laser axis. By relaying an image of the focal region onto a Rochester Optical Streak System camera, the expected focal-spot dynamics were verified, including subluminal and superluminal velocities, both forward and backward relative to the laser propagation [74]. Because several applications rely on ionization waves of arbitrary velocity (IWAVs), and the flying focus was predicted to produce suitable IWAVs [80], subsequent experiments have demonstrated this technique [81,82]. Using a setup similar to that described above but increasing the energy in the MTW pulse up to ~25 mJ, the peak intensity exceeded 10^{14} W/cm^2 at best focus and was sufficient to form IWAVs in ambient air. To diagnose the plasma-formation dynamics, a novel chirped Schlieren technique was developed using a frequency-doubled and optically delayed fraction of the same MTW beam. Although the resulting plasma channels were long (several mm), they were also very narrow (<10 µm), which could limit some applications [81]. To demonstrate additional flexibility, the final experiment increased the laser energy still farther (up to 5 J), such that the ionization threshold of the gas was reached in the quasi-far field. It was performed in the UDP chamber using the gas-jet platform for additional control over the ionization region and successfully demonstrated larger (several hundred µm diameter) plasma channels that still maintained the beneficial dynamics of the flying focus [82].

E. Raman Amplification

Parametric amplification using stimulated Raman scattering (SRS) in a plasma could provide the enabling technology in the generation of ultrahigh-power laser pulses. An experimental program is in development on the UDP chamber to study the amplification of a short 100 fs seed provided by the idler (~1175 nm) of the OPAL laser system counterpropagating

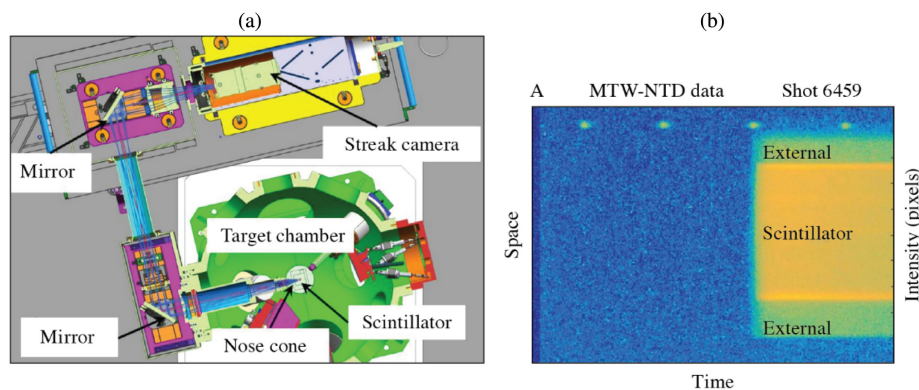

Fig. 25.   (a) CAD drawing of the MTW-NTD experimental setup. Light from the scintillator is transported through an optical relay system to the optical streak camera. (b) CCD image of the streak camera record from a MTW target shot.

with a 15 ps energetic pump ($\sim$1053 nm) provided by the MTW laser system. The first campaign of the program used Thomson scattering to study the evolution of the plasma density and temperature of the pump ionizing and propagating through a hydrogen gas cell near parameters relevant to Raman amplification ($n_e \sim 10^{19}$ cm^{-3}, $I_{pump} \sim 10^{14}$ W/cm^2) [83,84]. Unprecedented picosecond time resolution, enabled by a pulse-front-tilt-compensated spectrometer, showed a transition from an initially cold plasma to a quasistationary equilibrium temperature over $\sim$25 ps. It was determined that ionization-induced refraction of the front of the pump pulse, filamentation in the initially cold plasma, and a time-dependent detuning of the Raman scattering resonance due to heating are all detrimental to the production of an efficient Raman amplifier.

The second campaign demonstrated that it is possible to propagate the pump through a preformed plasma at Raman-relevant conditions without negative effects from ionization-induced refraction or filamentation. The UDP-E laser was focused with a 500 μm diameter distributed phase plate to both fully ionize and heat the gas jet to prevent ionization-induced refraction, filamentation, and resonance detuning. The elevated temperatures are also beneficial in preventing strong growth of other fluid limitations of Raman amplification, such as SRS growing ahead of the seed from noise.

Simultaneous work on developing a high-power seed (largely absent in previous experimental investigations of Raman amplification) at the appropriately shifted wavelength (1170 nm) is underway using the idler from the front end of the OPAL laser system. The system involves the development of a grism stretcher [85], angular dispersion compensator, and a compressor to achieve the design goals of 50 mJ in 115 fs. Full-scale Raman amplification experiments are planned at the completion of the seed-pulse development.

F. Fifth-Harmonic Generation

High-energy ultraviolet (UV) sources are required to probe hot dense plasmas from fusion experiments by using Thomson scattering resulting from the lower self-generated background from the plasma in the 180 to 230 nm spectral region [38]. The fifth harmonic of neodymium lasers at 211 nm fits that window. MTW was used to investigate high-efficiency 5HG in large-aperture crystals of cesium lithium borate (CLBO) [11], ammonium dihydrogen phosphate (ADP) [12], and beta barium borate (BBO) [86]. The laser operating in the narrowband mode and in under four round-trips in CLARA-produced square pulses from 1 to 2.8 ns with a flattop, square beam profile (12 mm × 12 mm). The pulse energy reached 1.5 J at 5 Hz or 0.1 Hz repetition rate as well as in a single-shot regime. The record conversion efficiency of 30% from fundamental frequency into 5ω has been realized in the CLBO crystal. Nonlinear absorption was demonstrated to be a major limiting factor.

5. CONCLUSION

MTW was built based on the most-recent laser technologies and continues to develop novel ideas in laser science and engineering. It is also a flexible platform to create frontier laser and plasma diagnostics. The output beam with size up to 70 mm × 70 mm, output energy up to 120 J and pulse duration from 20 fs to 2.8 ns can be directed to different chambers for various experiments, including development of an ultrahigh-intensity all-OPCPA system and a Raman plasma amplifier.

Disclosures. The authors declare no conflicts of interest.

Data Availability. Data underlying the results presented in this paper are not publicly available at this time but may be obtained from the authors upon reasonable request.

†Deceased.

REFERENCES

1. S. Gales, K. A. Tanaka, D. L. Balabanski, F. Negoita, D. Stutman, O. Tesileanu, C. A. Ur, D. Ursescu, I. Andrei, S. Ataman, M. O. Cernaianu, L. D'Alessi, I. Dancus, B. Diaconescu, N. Djourelov, D. Filipescu, P. Ghenuche, D. G. Ghita, C. Matei, K. Seto, M. Zeng, and N. V. Zamfir, "The extreme light infrastructure—nuclear physics (ELI-NP) Facility: New horizons in physics with 10 PW ultra-intense lasers and 20 MeV brilliant gamma beams," Rep. Prog. Phys. **81**, 094301 (2018).

2. A. L. Kritcher, D. C. Swift, T. Döppner, B. Bachmann, L. X. Benedict, G. W. Collins, J. L. DuBois, F. Elsner, G. Fontaine, J. A. Gaffney, S. Hamel, A. Lazicki, W. R. Johnson, N. Kostinski, D. Kraus, M. J. MacDonald, B. Maddox, M. E. Martin, P. Neumayer, A. Nikroo, J. Nilsen, B. A. Remington, D. Saumon, P. A. Sterne, W. Sweet, A. A. Correa, H. D. Whitley, R. W. Falcone, and S. H. Glenzer, "A measurements of the equation of state of carbon envelopes of white dwarfs," Nature **584**, 51–54 (2020).

3. G. H. Miller, E. I. Moses, and C. R. Wuest, "The National Ignition Facility," Opt. Eng. **43**, 2841–2853 (2004).

4. J. H. Kelly, L. J. Waxer, V. Bagnoud, I. A. Begishev, J. Bromage, B. E. Kruschwitz, T. J. Kessler, S. J. Loucks, D. N. Maywar, R. L. McCrory, D. D. Meyerhofer, S. F. B. Morse, J. B. Oliver, A. L. Rigatti, A. W. Schmid, C. Stoeckl, S. Dalton, L. Folnsbee, M. J. Guardalben, R. Jungquist, J. Puth, M. J. Shoup, III, D. Weiner, and J. D. Zuegel, "OMEGA EP: High-energy petawatt capability for the OMEGA Laser Facility," J. Phys. IV France **133**, 75–80 (2006).

5. J. Ebrardt and J. M. Chaput, "LMJ on its way to fusion," J. Phys. Conf. Ser. **244**, 032017 (2010).

6. C. N. Danson, P. A. Brummitt, R. J. Clarke, J. L. Collier, B. Fell, A. J. Frackiewicz, S. Hancock, S. Hawkes, C. Hernandez-Gomez, P. Holligan, M. H. R. Hutchinson, A. Kidd, W. J. Lester, I. O. Musgrave, D. Neely, D. R. Neville, P. A. Norreys, D. A. Pepler, C. J. Reason, W. Shaikh, T. B. Winstone, R. W. W. Wyatt, and B. E. Wyborn, "Vulcan Petawatt—An ultra-high-intensity interaction facility," Nucl. Fusion **44**, S239–S246 (2004).

7. G. Xu, T. Wang, Z. Li, Y. Dai, Z. Lin, Y. Gu, and J. Zhu, "1 kJ petawatt laser system for SG-II-U program," Rev. Laser Eng. **36**, 1172–1175 (2008).

8. V. V. Lozhkarev, G. I. Freidman, V. N. Ginzburg, E. V. Katin, E. A. Khazanov, A. V. Kirsanov, G. A. Luchinin, A. N. Mal'shakov, M. A. Martyanov, O. V. Palashov, A. K. Poteomkin, A. M. Sergeev, A. A. Shaykin, and I. V. Yakovlev, "Compact 0.56 petawatt laser system based on optical parametric chirped pulse amplification in KD*P crystals," Laser Phys. Lett. **4**, 421–427 (2007).

9. C. N. Danson, C. Haefner, J. Bromage, T. Butcher, J.-C. F. Chanteloup, E. A. Chowdhury, A. Galvanauskas, L. A. Gizzi, J. Hein, D. I. Hillier, N. W. Hopps, Y. Kato, E. A. Khazanov, R. Kodama, G. Korn, R. Li, Y. Li, J. Limpert, J. Ma, C. H. Nam, D. Neely, D. Papadopoulos, R. R. Penman, L. Qian, J. J. Rocca, A. A. Shaykin, C. W. Siders, C. Spindloe, S. Szatmári, R. M. G. M. Trines, J. Zhu, P. Zhu, and J. D. Zuegel, "Petawatt and exawatt class lasers worldwide," High Power Laser Sci. Eng. **7**, e54 (2019).

10. J. Bromage, S.-W. Bahk, I. A. Begishev, C. Dorrer, M. J. Guardalben, B. N. Hoffman, J. B. Oliver, R. G. Roides, E. M. Schiesser, M. J. Shoup, III, M. Spilatro, B. Webb, D. Weiner, and J. D. Zuegel, "Technology development for ultraintense all-OPCPA systems," High Power Laser Sci. Eng. **7**, e4 (2019).

11. I. A. Begishev, J. Bromage, S. T. Yang, P. S. Datte, S. Patankar, and J. D. Zuegel, "Record fifth-harmonic-generation efficiency producing 211 nm, joule-level pulses using cesium lithium borate," Opt. Lett. **43**, 2462–2465 (2018).

12. I. A. Begishev, G. Brent, S. Carey, R. Chapman, I. A. Kulagin, M. H. Romanofsky, M. J. Shoup, J. D. Zuegel, and J. Bromage, "High-efficiency, fifth-harmonic generation of a joule-level neodymium laser in a large-aperture ammonium dihydrogen phosphate crystal," Opt. Express **29**, 1879–1889 (2021).

13. J. R. Marciante, "Fiber technologies for terawatt lasers," presented at the Optical Fiber Communication Conference, Anaheim, California, March 25–29, 2007.

14. A. V. Okishev, D. J. Battaglia, I. A. Begishev, and J. D. Zuegel, "Highly stable, diode-pumped, cavity-dumped Nd:YLF regenerative amplifier for the OMEGA laser fusion facility," in *Advanced Solid-State Lasers*, M. E. Fermann and L. R. Marshall, eds., Vol. **68** of OSA Trends in Optics and Photonics Series, (Optical Society of America, 2002), pp. 418–422.

15. V. Bagnoud, M. J. Guardalben, J. Puth, J. D. Zuegel, T. Mooney, and P. Dumas, "High-energy, high-average-power laser with Nd:YLF rods corrected by magnetorheological finishing," Appl. Opt. **44**, 282–288 (2005).

16. C. Dorrer and J. D. Zuegel, "Design and analysis of binary beam shapers using error diffusion," J. Opt. Soc. Am. B **24**, 1268–1275 (2007).

17. C. Dorrer, I. A. Begishev, A. V. Okishev, and J. D. Zuegel, "High-contrast optical-parametric amplifier as a front end of high-power laser systems," Opt. Lett. **32**, 2143–2145 (2007).

18. C. Dorrer, A. Consentino, D. Irwin, J. Qiao, and J. D. Zuegel, "OPCPA front end and contrast optimization for the OMEGA EP kilojoule, picosecond laser," J. Opt. A **17**, 094007 (2015).

19. I. Musgrave, W. Shaikh, M. Galimberti, A. Boyle, C. Hernandez-Gomez, K. Lancaster, and R. Heathcote, "Picosecond optical parametric chirped pulse amplifier as a preamplifier to generate high-energy seed pulses for contrast enhancement," Appl. Opt. **49**, 6558–6562 (2010).

20. N. Hopps, C. Danson, S. Duffield, D. Egan, S. Elsmere, M. Girling, E. Harvey, D. Hillier, M. L. Norman, S. P. Parker, P. Treadwell, D. Winter, and T. H. Bett, "Overview of laser systems for the Orion facility at the AWE," Appl. Opt. **52**, 3597–3607 (2013).

21. F. Wagner, C. P. João, J. Fils, T. Gottschall, J. Hein, J. Körner, J. Limpert, M. Roth, T. Stöhlker, and V. Bagnoud, "Temporal contrast control at the PHELIX petawatt laser facility by means of tunable sub-picosecond optical parametric amplification," Appl. Phys. B **116**, 429–435 (2014).

22. E. Gaul, T. Toncian, M. Martinez, J. Gordon, M. Spinks, G. Dyer, N. Truong, C. Wagner, G. Tiwari, M. E. Donovan, T. Ditmire, and B. M. Hegelich, "Improved pulse contrast on the Texas Petawatt Laser," J. Phys. Conf. Ser. **717**, 012092 (2016).

23. J. E. Heebner, R. L. Acree, Jr., D. A. Alessi, A. I. Barnes, M. W. Bowers, D. F. Browning, T. S. Budge, S. Burns, L. S. Chang, K. S. Christensen, J. K. Crane, M. J. Dailey, G. V. Erbert, M. Fischer, M. Flegel, B. P. Golick, J. M. Halpin, M. Y. Hamamoto, M. R. Hermann,

V. J. Hernandez, J. Honig, J. A. Jarboe, D. H. Kalantar, V. K. Kanz, K. M. Knittel, J. R. Lusk, W. A. Molander, V. R. Pacheu, M. Paul, L. J. Pelz, M. A. Prantil, M. C. Rushford, N. Schenkel, R. J. Sigurdsson, T. M. Spinka, M. G. Taranowski, P. J. Wegner, K. C. Wilhelmsen, J. N. Wong, and S. T. Yang, "Injection laser system for advanced radiographic capability using chirped pulse amplification on the National Ignition Facility," Appl. Opt. **58**, 8501–8510 (2019).

24. C. Dorrer, R. G. Roides, J. Bromage, and J. D. Zuegel, "Self-phase modulation compensation in a regenerative amplifier using cascaded second-order nonlinearities," Opt. Lett. **39**, 4466–4469 (2014).

25. G. Chériaux, P. Rousseau, F. Salin, J. P. Chambaret, B. Walker, and L. F. Dimauro, "Aberration-free stretcher design for ultrashort-pulse amplification," Opt. Lett. **21**, 414–416 (1996).

26. I. V. Yakovlev, "Stretchers and compressors for ultra-high power laser systems," Quantum Electron. **44**, 393–414 (2014).

27. O. E. Martinez, "3000 times grating compressor with positive group velocity dispersion: Application to fiber compensation in 1.3–1.6 μm region," IEEE J. Quantum Electron. **23**, 59–64 (1987).

28. A. Dubietis, G. Jonusauskas, and A. Piskarskas, "Powerful femtosecond pulse generation by chirped and stretched pulse parametric amplification in BBO crystal," Opt. Commun. **88**, 437–440 (1992).

29. M. J. Guardalben, J. Keegan, L. J. Waxer, V. Bagnoud, I. A. Begishev, J. Puth, and J. D. Zuegel, "Design of highly stable, high-conversion-efficiency, optical parametric chirped-pulse amplification system with good beam quality," Opt. Express **11**, 2511–2524 (2003).

30. I. A. Begishev, V. Bagnoud, M. J. Guardalben, J. Puth, L. J. Waxer, and J. D. Zuegel, "Parasitic second-harmonic generation in optical parametric chirped-pulse amplification," in *Advanced Solid-State Photonics*, OSA Technical Digest (Optical Society of America, 2004), paper MB13.

31. I. A. Begishev, V. Bagnoud, C. Dorrer, and J. D. Zuegel, "Suppression of optical parametric generation in the high-efficient OPCPA system," in *Advanced Solid-State Photonics*, OSA Technical Digest Series (CD) (Optical Society of America, 2007), paper WD3.

32. V. Bagnoud, I. A. Begishev, M. J. Guardalben, J. Puth, and J. D. Zuegel, "5-Hz, >250-mJ optical parametric chirped-pulse amplifier at 1053 nm," Opt. Lett. **30**, 1843–1845 (2005).

33. V. Bagnoud and J. D. Zuegel, "Independent phase and amplitude control of a laser beam by use of a single-phase-only spatial light modulator," Opt. Lett. **29**, 295–297 (2004).

34. S.-W. Bahk, I. A. Begishev, and J. D. Zuegel, "Precompensation of gain nonuniformity in a Nd:glass amplifier using a programmable beam-shaping system," Opt. Commun. **333**, 45–52 (2014).

35. D. Broege, S. Fochs, G. Brent, J. Bromage, C. Dorrer, R. F. Earley, M. J. Guardalben, J. A. Marozas, R. G. Roides, I. Sethian, X. Wang, D. Weiner, J. Zweiback, and J. D. Zuegel, "The dynamic compression sector laser: A 100-J UV laser for dynamic compression research," Rev. Sci. Instrum. **90**, 053001 (2019).

36. C. R. Stillman, P. M. Nilson, S. T. Ivancic, I. E. Golovkin, C. Mileham, I. A. Begishev, and D. H. Froula, "Picosecond time-resolved measurements of dense plasma line shifts," Phys. Rev. E **95**, 063204 (2017).

37. D. Hillier, C. Danson, S. Duffield, D. Egan, S. Elsmere, M. Girling, E. Harvey, N. Hopps, M. Norman, S. Parker, P. Treadwell, D. Winter, and T. Bett, "Ultrahigh contrast from a frequency-doubled chirped-pulse-amplification beamline," Appl. Opt. **52**, 4258–4263 (2013).

38. J. S. Ross, S. H. Glenzer, J. P. Palastro, B. B. Pollock, D. Price, G. R. Tynan, and D. H. Froula, "Thomson-scattering measurements in the collective and noncollective regimes in laser produced plasmas," Rev. Sci. Instrum. **81**, 10D523 (2010).

39. V. V. Ivanov, A. A. Anderson, and I. A. Begishev, "Four-color laser diagnostics for Z-pinch and laser-produced plasma," Appl. Opt. **55**, 498–501 (2016).

40. J. Bromage, S. W. Bahk, M. Bedzyk, I. A. Begishev, S. Bucht, C. Dorrer, C. Feng, C. Jeon, C. Mileham, R. G. Roides, K. Shaughnessy, M. J. Shoup, M. Spilatro, B. Webb, D. Weiner, and J. D. Zuegel, "MTW-OPAL: A technology development platform for ultra-intense OPCPA systems," High Power Laser Sci. Eng. **9**, E63 (2021).

41. F. Salin, P. Georges, G. Roger, and A. Brun, "Single-shot measurement of a 52-fs pulse," Appl. Opt. **26**, 4528–4531 (1987).

42. C. Dorrer and J. Bromage, "Impact of high-frequency spectral phase modulation on the temporal profile of short optical pulses," Opt. Express **16**, 3058–3068 (2008).

43. J. Bromage, C. Dorrer, and R. K. Jungquist, "Temporal contrast degradation at the focus of ultrafast pulses from high-frequency spectral phase modulation," J. Opt. Soc. Am. B **29**, 1125–1135 (2012).

44. N. Forget, A. Cotel, E. Brambrink, P. Audebert, C. Le Blanc, A. Jullien, O. Albert, and G. Chériaux, "Pump-noise transfer in optical parametric chirped-pulse amplification," Opt. Lett. **30**, 2921–2923 (2005).

45. C. Dorrer, "Analysis of pump-induced temporal contrast degradation in optical parametric chirped-pulse amplification," J. Opt. Soc. Am. B **24**, 3048–3057 (2007).

46. I. N. Ross, G. H. C. New, and P. K. Bates, "Contrast limitation due to pump noise in an optical parametric chirped pulse amplification system," Opt. Commun. **273**, 510–514 (2007).

47. C. Dorrer, A. V. Okishev, I. A. Begishev, J. D. Zuegel, V. I. Smirnov, and L. B. Glebov, "Optical parametric chirped-pulse–amplification contrast enhancement by regenerative pump spectral filtering," Opt. Lett. **32**, 2378–2380 (2007).

48. C. Dorrer, A. Consentino, and D. Irwin, "Direct optical measurement of the on-shot incoherent focal spot and intensity contrast on the OMEGA EP laser," Appl. Phys. B **122**, 156 (2016).

49. M. E. Glinsky, "Regimes of suprathermal electron transport," Phys. Plasmas **2**, 2796–2806 (1995).

50. K. B. Wharton, S. P. Hatchett, S. C. Wilks, M. H. Key, J. D. Moody, V. Yanovsky, A. A. Offenberger, B. A. Hammel, M. D. Perry, and C. Joshi, "Experimental measurements of hot electrons generated by ultraintense (>1019 w/cm^2) laser-plasma interactions on solid-density targets," Phys. Rev. Lett. **81**, 822–825 (1998).

51. P. M. Nilson, J. R. Davies, W. Theobald, P. A. Jaanimagi, C. Mileham, R. K. Jungquist, C. Stoeckl, I. A. Begishev, A. A. Solodov, J. F. Myatt, J. D. Zuegel, T. C. Sangster, R. Betti, and D. D. Meyerhofer, "Time-resolved measurements of hot-electron equilibration dynamics in high-intensity laser interactions with thin-foil solid targets," Phys. Rev. Lett. **108**, 085002 (2012).

52. E. L. Clark, K. Krushelnick, M. Zepf, F. N. Beg, M. Tatarakis, A. Machacek, M. I. K. Santala, I. Watts, P. A. Norreys, and A. E. Dangor, "Energetic heavy-ion and proton generation from ultraintense laser-plasma interactions with solids," Phys. Rev. Lett. **85**, 1654–1657 (2000).

53. R. G. Evans, E. L. Clark, R. T. Eagleton, A. M. Dunne, R. D. Edwards, W. J. Garbett, T. J. Goldsack, S. James, C. C. Smith, B. R. Thomas, R. Clarke, D. J. Neely, and S. J. Rose, "Rapid heating of solid density material by a petawatt laser," Appl. Phys. Lett. **86**, 191505 (2005).

54. H.-S. Park, D. M. Chambers, H.-K. Chung, R. J. Clarke, R. Eagleton, E. Giraldez, T. Goldsack, R. Heathcote, N. Izumi, M. H. Key, J. A. King, J. A. Koch, O. L. Landen, A. Nikroo, P. K. Patel, D. F. Price, B. A. Remington, H. F. Robey, R. A. Snavely, D. A. Steinman, R. B. Stephens, C. Stoeckl, M. Storm, M. Tabak, W. Theobald, R. P. J. Town, J. E. Wickersham, and B. B. Zhang, "High-energy Kα radiography using high-intensity, short-pulse lasers," Phys. Plasmas **13**, 056309 (2006).

55. R. A. London and J. I. Castor, "Design of short pulse laser driven opacity experiments," High Energy Density Phys. **9**, 725–730 (2013).

56. B. A. Remington, D. Arnett, R. P. Drake, and H. Takabe, "Modeling astrophysical phenomena in the laboratory with intense lasers," Science **284**, 1488–1493 (1999).

57. O. V. Gotchev, P. Brijesh, P. M. Nilson, C. Stoeckl, and D. D. Meyerhofer, "A compact, multiangle electron spectrometer for ultraintense laser-plasma interaction experiments," Rev. Sci. Instrum. **79**, 053505 (2008).

58. P. M. Nilson, W. Theobald, J. Myatt, C. Stoeckl, M. Storm, O. V. Gotchev, J. D. Zuegel, R. Betti, D. D. Meyerhofer, and T. C. Sangster, "High-intensity laser-plasma interactions in the refluxing limit," Phys. Plasmas **15**, 056308 (2008).

59. J. R. Davies, R. Betti, P. M. Nilson, and A. A. Solodov, "Copper K-shell emission cross sections for laser–solid experiments," Phys. Plasmas **20**, 083118 (2013).

60. P. M. Nilson, W. Theobald, J. F. Myatt, C. Stoeckl, J. D. Zuegel, R. Betti, D. D. Meyerhofer, and T. C. Sangster, "X-ray spectroscopy of solid-density plasmas in high-intensity laser interactions," AIP Conf. Proc. **1161**, 17–23 (2009).

61. P. M. Nilson, A. A. Solodov, J. F. Myatt, W. Theobald, P. A. Jaanimagi, L. Gao, C. Stoeckl, R. S. Craxton, J. A. Delettrez, B. Yaakobi, J. D. Zuegel, B. E. Kruschwitz, C. Dorrer, J. H. Kelly, K. U. Akli, P. K. Patel, A. J. Mackinnon, R. Betti, T. C. Sangster, and D. D. Meyerhofer, "Scaling hot-electron generation to high-power, kilojoule-class laser–solid interactions," Phys. Rev. Lett. **105**, 235001 (2010).

62. P. M. Nilson, A. A. Solodov, J. F. Myatt, W. Theobald, P. A. Jaanimagi, L. Gao, C. Stoeckl, R. S. Craxton, J. A. Delettrez, B. Yaakobi, J. D. Zuegel, B. E. Kruschwitz, C. Dorrer, J. H. Kelly, K. U. Akli, P. K. Patel, A. J. Mackinnon, R. Betti, T. C. Sangster, and D. D. Meyerhofer, "Scaling hot-electron generation to long-pulse, high-intensity laser–solid interactions," Phys. Plasmas **18**, 056703 (2011).

63. P. M. Nilson, A. A. Solodov, J. R. Davies, W. Theobald, C. Mileham, C. Stoeckl, I. A. Begishev, J. D. Zuegel, D. H. Froula, R. Betti, and D. D. Meyerhofer, "Time-resolved Kα spectroscopy measurements of hot-electron equilibration dynamics in thin-foil solid targets: Collisional and collective effects," J. Phys. B **48**, 224001 (2015).

64. M. Storm, I. A. Begishev, R. J. Brown, C. Guo, D. D. Meyerhofer, C. Mileham, J. F. Myatt, P. M. Nilson, T. C. Sangster, C. Stoeckl, W. Theobald, and J. D. Zuegel, "A high-resolution coherent transition radiation diagnostic for laser-produced electron transport studies," Rev. Sci. Instrum. **79**, 10F503 (2008).

65. M. Storm, A. A. Solodov, J. F. Myatt, D. D. Meyerhofer, C. Stoeckl, C. Mileham, R. Betti, P. M. Nilson, T. C. Sangster, W. Theobald, and C. Guo, "High-current, relativistic electron-beam transport in metals and the role of magnetic collimation," Phys. Rev. Lett. **102**, 235004 (2009).

66. P. M. Nilson, W. Theobald, J. F. Myatt, C. Stoeckl, M. Storm, J. D. Zuegel, R. Betti, D. D. Meyerhofer, and T. C. Sangster, "Bulk heating of solid-density plasmas during high-intensity-laser plasma interactions," Phys. Rev. E **79**, 016406 (2009).

67. S. T. Ivancic, C. R. Stillman, D. Nelson, I. A. Begishev, C. Mileham, P. M. Nilson, and D. H. Froula, "Design of an extreme ultraviolet spectrometer suite to characterize rapidly heated solid matter," Rev. Sci. Instrum. **87**, 11E538 (2016).

68. C. R. Stillman, P. M. Nilson, S. T. Ivancic, C. Mileham, I. A. Begishev, R. K. Jungquist, D. J. Nelson, and D. H. Froula, "A streaked x-ray spectroscopy platform for rapidly heated, near-solid density plasmas," Rev. Sci. Instrum. **87**, 11E312 (2016).

69. P. M. Nilson, W. Theobald, C. Mileham, C. Stoeckl, J. F. Myatt, J. A. Delettrez, J. MacFarlane, I. A. Begishev, J. D. Zuegel, R. Betti, T. C. Sangster, and D. D. Meyerhofer, "Target-heating effects on the K$_{\alpha 1,2}$-emission spectrum from solid targets heated by laser-generated hot electrons," Phys. Plasmas **18**, 042702 (2011).

70. C. R. Stillman, P. M. Nilson, A. B. Sefkow, S. T. Ivancic, C. Mileham, I. A. Begishev, and D. H. Froula, "Energy transfer dynamics in strongly inhomogeneous hot-dense-matter systems," Phys. Rev. E **97**, 063208 (2018).

71. W. Theobald, V. Ovchinnikov, S. Ivancic, B. Eichman, P. M. Nilson, J. A. Delettrez, R. Yan, G. Li, F. J. Marshall, D. D. Meyerhofer, J. F. Myatt, C. Ren, T. C. Sangster, C. Stoeckl, J. D. Zuegel, L. Van Woerkom, R. R. Freeman, K. U. Akli, E. Giraldez, and R. B. Stephens, "High-intensity laser-plasma interaction with wedge-shaped-cavity targets," Phys. Plasmas **17**, 103101 (2010).

72. C. Stoeckl, W. Theobald, T. C. Sangster, M. H. Key, P. Patel, B. B. Zhang, R. Clarke, S. Karsch, and P. Norreys, "Operation of a single-photon–counting x-ray charge-coupled device camera spectrometer in a petawatt environment," Rev. Sci. Instrum. **75**, 3705–3707 (2004).

73. C. Stoeckl, R. Boni, F. Ehrne, C. J. Forrest, V. Yu. Glebov, J. Katz, D. J. Lonobile, J. Magoon, S. P. Regan, M. J. Shoup, III, A. Sorce, C. Sorce, T. C. Sangster, and D. Weiner, "Neutron temporal diagnostic for high-yield deuterium–tritium cryogenic implosions on OMEGA," Rev. Sci. Instrum. **87**, 053501 (2016).

74. D. H. Froula, D. Turnbull, A. S. Davies, T. J. Kessler, D. Haberberger, J. P. Palastro, S.-W. Bahk, I. A. Begishev, R. Boni, S. Bucht, J. Katz, and J. L. Shaw, "Spatiotemporal control of laser intensity," Nat. Photonics **12**, 262–265 (2018).

75. A. Sainte-Marie, O. Gobert, and F. Quéré, "Controlling the velocity of ultrashort light pulses in vacuum through spatio-temporal couplings," Optica **4**, 1298–1304 (2017).

76. D. Turnbull, S. Bucht, A. Davies, D. Haberberger, T. Kessler, J. L. Shaw, and D. H. Froula, "Raman amplification with a flying focus," Phys. Rev. Lett. **120**, 024801 (2018).

77. D. Turnbull, S.-W. Bahk, I. A. Begishev, R. Boni, J. Bromage, S. Bucht, A. Davies, P. Franke, D. Haberberger, J. Katz, T. J. Kessler, A. L. Milder, J. P. Palastro, J. L. Shaw, and D. H. Froula, "Flying focus and its application to plasma-based laser amplifiers," Plasma Phys. Controlled Fusion **61**, 014022 (2019).

78. A. Howard, D. Turnbull, A. S. Davies, P. Franke, D. H. Froula, and J. P. Palastro, "Photon acceleration in a flying focus," Phys. Rev. Lett. **123**, 124801 (2019).

79. J. P. Palastro, J. L. Shaw, P. Franke, D. Ramsey, T. T. Simpson, and D. H. Froula, "Dephasingless laser wakefield acceleration," Phys. Rev. Lett. **124**, 134802 (2020).

80. J. P. Palastro, D. Turnbull, S.-W. Bahk, R. K. Follett, J. L. Shaw, D. Haberberger, J. Bromage, and D. H. Froula, "Ionization waves of arbitrary velocity driven by a flying focus," Phys. Rev. A **97**, 033835 (2018).

81. D. Turnbull, P. Franke, J. Katz, J. P. Palastro, I. A. Begishev, R. Boni, J. Bromage, A. L. Milder, J. L. Shaw, and D. H. Froula, "Ionization waves of arbitrary velocity," Phys. Rev. Lett. **120**, 225001 (2018).

82. P. Franke, D. Turnbull, J. Katz, J. P. Palastro, I. A. Begishev, J. Bromage, J. L. Shaw, R. Boni, and D. H. Froula, "Measurement and control of large diameter ionization waves of arbitrary velocity," Opt. Express **27**, 31978–31988 (2019).

83. A. S. Davies, D. Haberberger, J. Katz, S. Bucht, J. P. Palastro, W. Rozmus, and D. H. Froula, "Picosecond thermodynamics in underdense plasmas measured with Thomson scattering," Phys. Rev. Lett. **122**, 155001 (2019).

84. A. S. Davies, D. Haberberger, J. Katz, S. Bucht, J. P. Palastro, R. K. Follett, and D. H. Froula, "Investigation of picosecond thermodynamics in a laser-produced plasma using Thomson-scattering," Plasma Phys. Controlled Fusion **62**, 014012 (2020).

85. S. Bucht, D. Haberberger, J. Bromage, and D. H. Froula, "Methodology for designing grism stretchers for idler-based optical parametric chirped-pulse-amplification systems," J. Opt. Soc. Am. B **36**, 2325–2337 (2019).

86. I. A. Begishev, V. V. Ivanov, S. Patankar, P. S. Datte, S. T. Yang, J. D. Zuegel, and J. Bromage, "Nonlinear crystals for efficient high-energy fifth- harmonic generation of near-IR lasers," in *Conference on Lasers and Electro-Optics*, OSA Technical Digest (Optical Society of America, 2020), paper SW3E.2.